The impact of coarse-grain protrusion on near-bed hydrodynamics

David Raus, Frédéric Moulin, Olivier Eiff

JGR Earth Surface

The Impact of Coarse-Grain Protrusion on Near-Bed Hydrodynamics

Key Points:

- The local hydrodynamics over fixed small grains for varying protrusion of immobile coarse grains, modeled by hemispheres, is investigated via particle image velocimetry
- A strong increase of the local shear stress for small protrusion levels around 20% is observed, which Raupach's drag partition model cannot predict
- For protrusion levels higher than about 50%, a reduction of the turbulent normal and shear stresses as well as the latter's quadrant distribution is observed, all suggesting reduced grain mobility

David Raus[1], Frédéric Yann Moulin[1], and Olivier Eiff[2]

[1]Institut de Mécanique des Fluides de Toulouse, Université de Toulouse, CNRS-Toulouse, Toulouse, France, [2]Karlsruher Institut für Technologie, Karlsruhe, Germany

Abstract In steep rivers, sediment is often transported over immobile cobbles and boulders. Previous studies of such conditions have observed that the entrainment rate of the mobile sediment strongly depends on the level of protrusion of the immobile grains. Here experiments are conducted in a laboratory flume in order to quantify how different levels of protrusion of large aggregates above a fixed fine-sediment bed, modeled as a patch of hemispheres, modify the local hydrodynamics near the fine-sediment bed. Five protrusion levels defined by $P = k/R = \{0\%, 20\%, 40\%, 60\%, 80\%\}$ were investigated, where k is the protrusion height and R the radius. For small protrusion ($P = 20\%$), enhanced shear stress and turbulence intensity on the fine-sediment bed is observed as the mixing layer generated at the hemisphere top impacts the fine-sediment bed. Moreover, sweep events generated near the top of the hemispheres reach the fine-sediment bed. For large protrusions ($P \geq 60\%$), the mixing layer generated near the top of the hemispheres does not reach the fine grains with the consequence that the shear stress drops. The remaining turbulence near the fine-sediment bed, although enhanced by the wakes generated by the hemispherical caps, is quasi-isotropic. The transition between these two distinct near-bed flow regimes is found to be around $P = 40\%$, corresponding to the protrusion levels observed by Grams and Wilcock (2014, https://doi.org/10.1002/2013JF002925) above which the erosion of fine sediment ceases.

1. Introduction

Wide grain-size distributions can cause predicted bed-load transport rates to be inaccurate (e.g., Yager et al., 2007). If the sediment bed consists of bimodal granular media with a large size ratio, segregation of the granular media can lead larger aggregates to move toward the surface and protrude through the finer sediment. Thus, stream beds often consist of fine sediment being transported over coarse aggregates including large gravel, cobbles, or boulders, which are not set into motion by the flow except by extreme events. Clearly, the motion of the finer grains inside the interfacial sublayer of the immobile aggregates depends on the level of protrusion and spatial density of the aggregates. The interfacial sublayer is the flow region below the top of the aggregates or roughness elements, following the definition of Nikora et al. (2001). While the presence of large aggregates increases the total shear stress acting on the bed composed of aggregates and fine-sediment flow (i.e., the flow resistance), it is not fully available to set the finer sediment in motion (Einstein & Banks, 1950; Raupach et al., 1993; Smith & McLean, 1977; Yager et al., 2007). Most of the total shear stress is spent on the form drag of the larger aggregates, while only a small portion remains for the fine-sediment bed. Such drag partition was proposed early on in the context of eolian canopies without sediment by Marshall (1971) who measured the stress partitioning in a wind tunnel and Raupach (1992) who developed a partitioning model.

Numerous authors use spatial averaging of the turbulent and mean velocities in order to analyze the three-dimensional mean flow inside the roughness sublayer (e.g., Florens et al., 2013; Nikora et al., 2001) in a one-dimensional manner. Pokrajac et al. (2006), for instance, describe how the time- and space-averaged total shear stress varies with elevation above the bed, exhibiting a maximum value at elevations near the crest of the roughness element and decreasing below the crest as fluid momentum is increasingly transferred to the roughness elements through form and viscous drag. The shear stress acting on the bed at the bottom of the interfacial sublayer (i.e., on the fine-sediment bed) is thus weaker than the total shear stress. This is particularly important for low submerged flows.

The effect of the presence of immobile roughness elements on sediment transport was first studied in aeolian conditions. Gillette and Stockton (1989) and Iversen et al. (1991) investigated the protection effect of immo-

bile coarse inclusions on transport by saltation. They showed that, for a fixed level of exposure of the coarse inclusions, the threshold friction velocity (that is required for particle motion) increases with the planar density of the coarse inclusions, indicating a protection or sheltering effect. Laboratory studies (Al-Awadhi & Willetts, 1999) and field studies (Gillies et al., 2006) have confirmed these observations. In rivers with a poorly sorted sediment bed, this increase of the threshold friction velocity is also observed (Schneider et al., 2015). Ferguson (2012) found that this increase of the threshold friction velocity has a clear dependence on the d_{84}/d_{50} ratio, where d_{84} and d_{50} are the particle sizes for which 84% and 50% of the sediment is finer, respectively. For a poorly sorted river sediment bed, Wiberg and Smith (1991) argue that the critical shear stress of the larger grains can be lower than that of the finer material because coarse grains on a fine bed will have relatively lower intergranular friction angles and are more exposed to the mean flow. The authors conclude that, consequently, the fine sediment can be set in motion once the coarser grains move, exposing the fine sediment to the flow and increasing the near-bed shear stress due to the absence of form drag associated with the coarse grains. However, the authors note that the finest grains are also affected by the turbulent velocity fluctuations in the wake of the coarse grains, which can set the fine grains in motion through turbulent sweeps of the bed.

Other authors have focused more specifically on the flow conditions before the coarse grains are set in motion. In a laboratory study, Yager et al. (2007) investigated bedload transport over immobile roughness elements in a steep channel by varying the surface density of an array of staggered immobile spheres. The authors observed that the entrainment rate of finer particles decreases by increasing the level of protrusion of the large immobile spheres or by increasing their spatial density. Grams and Wilcock (2007, 2014) studied suspended sediment transport over a layer of immobile coarse hemispheres. It appeared that transport occurred in two main modes: (1) patches of fine sediment fully covering the immobile elements and (2) entrainment of fine sediment in the interstitial spaces between the hemispheres. The results showed a strong dependence of fine-sediment transport on the protrusion level of the hemispheres.

This dependence of sediment entrainment on the level of protrusion of immobile roughness elements is not fully understood. Nickling and McKenna Neuman (1995) studied aeolian transport of fine sediment by saltation over a layer of immobile spheres, the spheres being initially fully covered by the sediment. The authors observed that when the immobile spheres start protruding, the sediment entrainment increases, in agreement with increasing total shear stress, and then decreases below the no-protrusion rate as the spheres are progressively exposed. This suggests competing sheltering and drag partitioning effects. Similarly, Grams and Wilcock (2007) measured the near-bed entrainment rate of fine sediment for different levels of protrusion of a layer of large hemispheres. They observed that the entrainment rate first increases for small protrusions and then decreases as the protrusion increases further, concluding that the transition in transport rates occurs when the large hemispheres protrude enough to shelter the sediment. Erosion was observed to persist for protrusion levels up to 50%. The explanation given by the authors is that the near-bed turbulence generated in the wake of the immobile hemispheres creates a locally strong increase of the bed shear stress, leading to enhanced transport. The same explanation was invoked in more recent experimental studies of Wren et al. (2011) and Grams and Wilcock (2014).

There are also bed configurations where the near-bed turbulence intensity (i.e., the normal stresses) increases, which can enhance the mobility and transport of fine sediments even if the bed shear stress decreases. Sutton and McKenna Neuman (2008b), for instance, observed such a variation of the ratio of normal stress to bed shear stress for flow around an array of cylinders on a smooth bed without particles. The influence of the near-bed turbulence intensity on sediment transport was investigated by Sumer et al. (2003). They showed that sediment entrainment is strongly dependent on the turbulence intensity near the bed when the turbulence is generated by an external source (as, e.g., the wake of an obstacle). Empirical sediment transport laws depending on the near-bed turbulence level have been suggested by Sumer et al. (2003), successfully applied for scour around an isolated hemisphere (Dixen et al., 2013) but not applied yet for the case of sediment transport in an array of immobile roughness elements where turbulence can also be enhanced due to the wakes of the immobile elements.

However, even for turbulent flows over homogeneous beds, grains are not set in motion by the time-averaged bed shear stress $\overline{u'w'}$ but by instantaneous events near the bed that can create locally strong velocity fluctuation cross products ($u'w'$) which are washed out when averaged (Sechet & le Guennec, 1999). In particular, a strong correlation between intense sweep events ($u'w' < 0$ with $u' > 0$ and $w' < 0$) near the bed

and sediment transport is observed (Nelson et al., 1995). Thus, the transport of fine sediments in an array of large immobile roughness elements is very likely to be subject to modifications of the instantaneous events reaching the fine-sediment bed since the generation of coherent flow structures is influenced by the bed roughness. For instance, coarse gravel has been shown to be responsible for an increase of sweeps near the fine-sediment bed, which could trigger fine grain motions (Hardy et al., 2010; Nelson et al., 2001). Similar effects are also suggested by the study of Chang et al. (2011) who investigated sediment transport in the lee of an obstacle. These authors showed that using the time-averaged bed shear stress underestimates the entrainment rate for flow around an in-stream rectangular cylinder at low angles of attack by a factor 2 to 3 compared with that estimated from the instantaneous bed shear stress. Finally, Papanicolaou et al. (2001) show how the generation of coherent flow structures is influenced by the spatial density of the bed roughness elements, with the frequency of the generation of turbulent-burst structures increasing as the density of bed roughness elements increases. Such modifications of the near-bed velocity time series would clearly impact the transport properties of the flow for fine sediment.

The goal of this study is to understand how the level of protrusion of an array of immobile large aggregates modifies the hydrodynamics near the fine-sediment bed. To this end, the flow is modeled in an open-channel flume using a patch of hemispheres at different levels of protrusion above a fixed bed of fine sediment (glued grains). Using particle image velocimetry (PIV) measurements, mean flow and turbulence statistics are obtained above the hemispheres as well as inside the interfacial sublayer, resolved down to the fine-sediment scale. For different levels of protrusion of the patch of hemispheres, the local bed-shear stress over the fine sediment as well as the local near-bed turbulence statistics are compared with the no-protrusion case.

The experimental setup and PIV measurements are presented in section 2. The main features of the three-dimensional mean flow and the roughness sublayer structure are presented and discussed in section 3. In section 4, the local mean and turbulent hydrodynamics near the fixed fine-sediment bed between the protruding hemispheres is investigated. The relevance of these purely hydrodynamical results to help explain the fine-sediment transport rates observed in experiments conducted by others is discussed in section 5. Conclusions and perspectives are drawn in section 6. In Appendix A, complementary results from a quadrant analysis performed near the fine-sediment bed and near the hemispheres' top are presented, showing how the penetration of coherent structures inside the interfacial sublayer evolves with the protrusion level.

2. Experimental Setup

The experiments were conducted in an 11-m-long, 0.5-m-wide, 0.2-m-deep horizontal flume at the Institut de Mécanique des Fluides de Toulouse. The bed was covered by glued fine sediment from 2.3 m upstream of the measurement section up to 0.45 m downstream (Figure 1a). The glued fine sediment was made of plastic particles with $d_{50} = 2.2$ mm and $d_{90} = 2.9$ mm, where d_{90} is the particle size for which 90% of the sediment is finer. In the measurement section, four patches of 3-D-printed spherical caps were screwed onto the immobile fine-sediment bed, and four scenarios were examined (details below). The caps had a radius $R = 2$ cm and were fixed in a square arrangement of 7×5 caps plus a final row of five caps, as illustrated in Figure 1c, with a spacing $l = 4.5\,\text{cm} = 2.25R$. The square arrangement was chosen so that PIV measurements (see below) down to the fine-sediment bed could be performed without the caps blocking the view of the instrument, at least in the alleys between the spherical caps.

The protrusion P of a spherical cap is defined as the ratio of the protruding height k above the fine-grained sediment bed to the full vertical radius R of the spherical cap:

$$P = \frac{k}{R}, \tag{1}$$

where $P = 100\%$ corresponds to a completely uncovered hemisphere. In each patch, all the spherical caps have the same protrusion level for five different cases ($P = 0\%$, $P = 20\%$, $P = 40\%$, $P = 60\%$, and $P = 80\%$). Measurements at $P = 0\%$ represent those for the glued fine-sediment bed without any caps.

The x, y, and z axes are defined, respectively, as the streamwise, transverse, and vertical directions. Here $z = 0$ is taken at the average position of the fine-sediment flow interface as measured by the PIV camera (see Figure 1b). The water depth D, measured between the fine-sediment bed position $z = 0$ and the water surface, is maintained constant for all experiments with a value of $D = 0.125$ m.

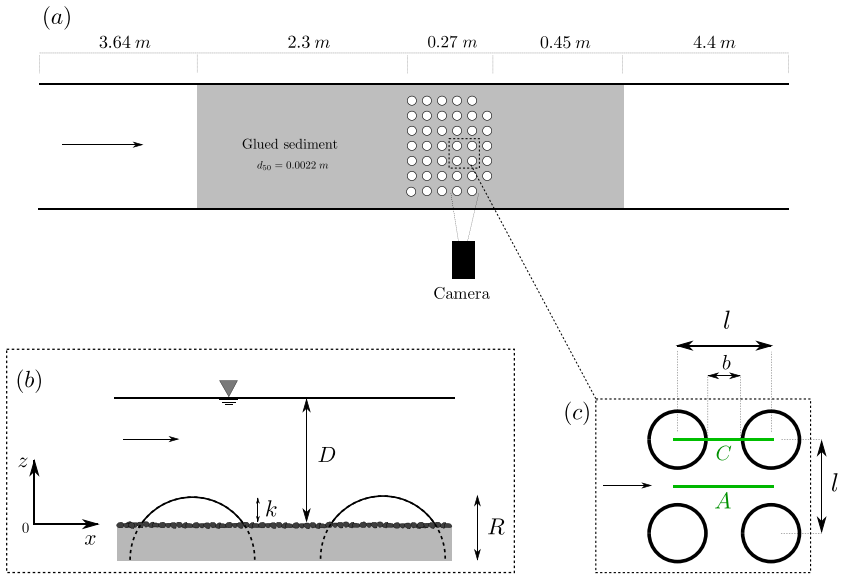

Figure 1. (a) Top view of the flume and positions of the patch of spherical caps (white circles) and glued sediment (gray shaded). (b) Zoomed side view of the patch. (c) Top view of an elemental pattern of spherical caps and positions of the laser sheets, A and C.

Instantaneous velocity fields were obtained by performing PIV measurements with a 16-bit high-resolution PCO Edge camera with a sensor size $2,160 \times 2,560$ pixels, in two wall-normal flow-parallel planes: plane C in the center of the patch of hemispheres, crossing two crests of the caps, and plane A in the adjoining downstream alley between the spherical caps (see Figure 1c). With the chosen camera angle, two hidden zones were present in plane A, since the spherical caps blocked the near bed region. The PIV fields were centered between the fourth row and the fifth row of spherical caps, where the flow is assumed to be fully developed inside the interfacial sublayer. The flow was seeded with 10-µm Dantec hollow glass spheres and illuminated with a laser-sheet generated by a 2×30 mJ Nd:Yag Quantel Twins Ultra laser and introduced via a set of mirrors from above. In order to reduce laser-sheet fluctuations, the sheet penetrated the free surface through a very slender glass window skimming the water surface, minimizing flow disturbances. To assure statistical convergence of the measurements, 5,000 statistically independent instantaneous velocity fields were recorded at the frequency $f = 3$ Hz for each case. The velocity fields were computed via an in-house software (CPIV-IMFT), with 16×16 pixels interrogation boxes with 50% overlap, the resolution of the images being 0.024 mm per pixel. The grid spacing was therefore 0.2 mm.

The bulk velocity is defined as $U_b = Q/(BD)$, where $B = 50$ cm is the width of the flume and Q the water discharge. Three discharges were investigated, $Q = \{6.6, 9.2, 13.7\}$ L/s, for each of the five protrusion levels $P = \{0, 20, 40, 60, 80\}$%; see Table 1. The flow discharge Q was chosen in order to obtain fully rough turbulent flow conditions. Two Reynolds numbers (also in Table 1) can be defined:

$$Re_D = U_b D/\nu, \tag{2}$$

$$Re_k = U_k k/\nu, \tag{3}$$

where U_k is the double-averaged (i.e., temporal and spatial averaging in the horizontal directions) longitudinal velocity at the spherical caps' top ($z = k$) and ν the kinematic viscosity of the fluid.

The chosen water depth D and the hemisphere's radius R are close to the values in Graba et al. (2010), where flow uniformity in the transverse direction in the same flume was verified. As in this earlier study, the effective channel-width to water-depth aspect ratio, $B/(D-k)$, is above 4. Combined with the fully rough beds, the flow near the center of the channel is therefore only weakly affected by the secondary currents generated by the lateral walls and is so essentially two-dimensional. The radius R of the hemispheres was chosen to keep the relative submergence D/k for the highest protrusion ($P = 80$%) high enough to avoid low

Table 1
Experimental Parameters

Experiment	P (%)	k (m)	D/k	λ_f	λ_p	Q (L/s)	U_b (cm/s)	Fr	$Re_D \times 10^3$	Re_k
P0Q14	0	0	0	0	0	13.7	22.4	0.202	27.7	—
P20Q14	20	0.004	31.3	0.032	0.22	13.7	22.4	0.204	27.7	489
P40Q14	40	0.008	15.6	0.088	0.40	13.7	22.4	0.206	27.7	1027
P60Q14	60	0.012	10.4	0.16	0.52	13.7	22.4	0.210	27.7	1449
P80Q14	80	0.016	7.8	0.23	0.60	13.7	22.4	0.213	27.7	2191
P0Q9	0	0	0	0	0	9.2	15.0	0.136	18.6	—
P20Q9	20	0.004	31.3	0.032	0.22	9.2	15.0	0.137	18.6	345
P40Q9	40	0.008	15.6	0.088	0.40	9.2	15.0	0.138	18.6	685
P60Q9	60	0.012	10.4	0.16	0.52	9.2	15.0	0.141	18.6	1157
P80Q9	80	0.016	7.8	0.23	0.60	9.2	15.0	0.143	18.6	1427
P0Q7	0	0	0	0	0	6.6	10.8	0.097	13.3	—
P20Q7	20	0.004	31.3	0.032	0.22	6.6	10.8	0.098	13.3	253
P40Q7	40	0.008	15.6	0.088	0.40	6.6	10.8	0.099	13.3	481
P60Q7	60	0.012	10.4	0.16	0.52	6.6	10.8	0.101	13.3	834
P80Q7	80	0.016	7.8	0.23	0.60	6.6	10.8	0.102	13.3	993

Note. $P = k/R$ is the protrusion; k is the caps' protrusion height; D/k is the relative submergence with D the water depth; $\lambda_f = nS_f/S$ is the frontal density and $\lambda_p = nS_p/S$ is the planar density with n the number of roughness elements of frontal area S_f and plane area S_p covering the surface S; Q is the discharge; $U_b = Q/(BD)$ is the bulk velocity; $Fr = U_b/\sqrt{gD}$ is the Froude number; $Re_D = U_b D/\nu$ is the bulk Reynolds number; and $Re_k = U_k k/\nu$ is the crest Reynolds number.

submergence effects. In Rouzes et al. (2018), low submergence effects are observed in the log law parameters with an array of cubes for D/k below 6.7, with values of the hydraulic roughness k_s diverging from values found in highly submerged flow conditions. With $R = 2$ cm chosen here, the lowest D/k was equal to 7.8 so that all protrusions can be considered highly submerged. For the fine sediment, a scale separation with the hemispheres of at least one decade seemed reasonable to allow investigation of the spherical caps' interfacial layer without penetrating inside the fine sediment's roughness sublayer. Roughness sublayers are the highly inhomogeneous flow regions consisting of the interfacial sublayer and form-induced sublayer above the roughness elements, here the spherical caps or fine-sediment grains, and their thickness scales with the roughness element's vertical extent, that is, k or d_{50}, respectively. With $d_{50} = 2.2$ mm and a PIV spatial resolution of 0.2 mm, the spatial variations of the near-bed fine-sediment flow conditions inside the spherical caps' interfacial sublayer are investigated with a minimum of 20 measurement levels between the near-bed sediment and spherical caps' top for the lowest protrusion of $P = 20\%$ ($k = 4$mm). More quantitative analysis of the roughness sublayer thicknesses will be performed and discussed in the following sections.

3. Flow Structure

3.1. Time-Averaged Flow Fields

Figures 2a–2e and 2f–2j show the time-averaged longitudinal and vertical velocity fields, respectively, with superposed streamlines in the interfacial sublayer, for all levels of protrusion $P = \{0, 20, 40, 60, 80\}\%$. For $P = 20\%$, a recirculation is created in the wake of the spherical cap. This recirculation bubble is shorter than the distance between two spherical caps so that the spherical caps remain fully exposed to the free stream flow. For $P = \{40, 60, 80\}\%$, the reattachment point of the recirculation, defined here as the position of zero streamwise and vertical velocity, is on the downstream spherical cap's surface. The reattachment position relative to the crest for $P \geq 40\%$ is not dependent on the protrusion, implying that the portion of the spherical caps exposed to the outer flow is independent of the protrusion. It also appears that the magnitude of the mean vertical velocity between the spherical caps depends on the distance at the base between them, the mean vertical velocity being minimum for $P = 20\%$ where the recirculation bubble is not limited by the next spherical cap. Depending on the level of interaction of the roughness elements with the flow, Morris (1955) delimits three regimes: isolated; wake interference, and skimming flow. In the case of urban canopies (i.e., rough beds of building-like cubes or cuboids), Grimmond and Oke (1999) show that for planar densities of roughness elements $\lambda_p < 0.15$ (where $\lambda_p = nS_p/S$ with n the number of roughness elements

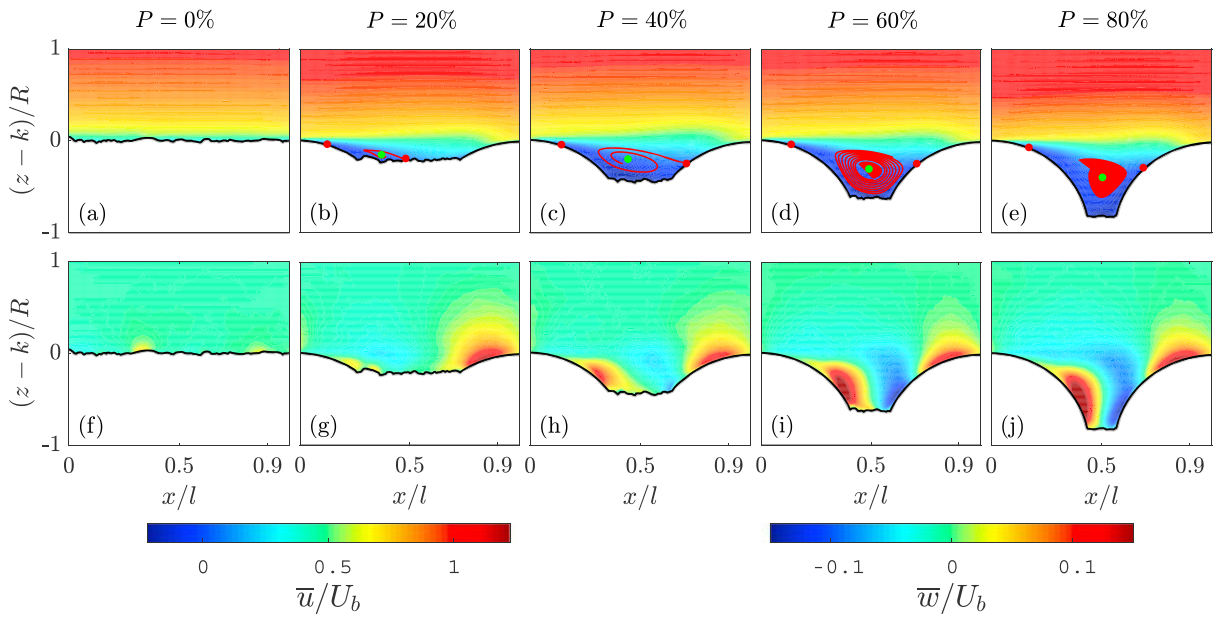

Figure 2. Dimensionless mean velocity fields for $Re_D = 27,700$ (experiments PXXQ14) in plane C for all five protrusion levels $P = 0$–80%, with (a–e) streamwise velocity and (f–j) vertical velocity. The red dots show the position of the separation and reattachment points, and the green dots show the position of the center of the vortex. The overbar denotes time averaging.

of planar area S_p covering the surface S), the interaction between each roughness element and the flow is strong, as the roughness elements are fully exposed to the flow and act as wake generators, corresponding to the isolated regime. For $0.15 < \lambda_p < 0.35$, referred to as the wake-interference flow regime, the sheltering effect between the roughness elements becomes strong, and the momentum exchange between the roughness elements and the flow weakens. Finally, for $\lambda_p > 0.35$, referred to as the skimming flow regime, a stable vortex forms and the interaction between the roughness elements and the outer flow diminishes further. A study of these three regimes for the specific case of spherical roughness elements was performed by Papanicolaou et al. (2001).

The planar densities for the nonzero protrusions $P = \{20, 40, 60, 80\}\%$ are $\lambda_p = \{0.22, 0.40, 0.52, 0.60\}$, respectively (see Table 1). For $P = 20\%$, the flow topology suggests that the flow regime is still wake dominated (the isolated regime) since the wake generated by a spherical cap impacts the fine-sediment bed before reaching the next cap. Yet, since $\lambda_p = 0.22$, the criterion $\lambda_p > 0.15$ is satisfied for which the wake interference regime is expected, at least for urban canopies made of cuboid roughness elements. However, spherical caps for $P = 20\%$ are rounded objects with a wake topology clearly different from cuboids even at the same value of λ_p. Therefore, for the bed of spherical caps, it is not impossible that the first transition proposed by Grimmond and Oke (1999) occurs for a protrusion between $P = 20\%$ and $P = 40\%$, that is, for λ_p between 0.22 and 0.40.

Figure 3 shows the local shear stress $\tau_{xz}|_{\text{local}} = \mu(\partial\bar{u}/\partial z) - \rho_f \overline{u'w'}$ in planes C and A normalized by $\rho_f u_\star^2$, where $\bar{u}$ is the time averaged streamwise velocity, u' and w' are the turbulent velocity fluctuations, $u_\star$ is the friction velocity and μ and ρ_f are the viscosity and density of the fluid, respectively. We use here the term local to emphasize the fact that the shear stress is not spatially averaged. The friction velocity $u_\star$ scales the turbulence acting at the top of the caps, with the scaling of the turbulence further discussed in section 3.3. For the no-protrusion case $P = 0\%$, the inhomogeneities in the Reynolds shear stress reflect still-limited time convergence of the measurements (see next subsection). When the caps are present, the main contribution to the total shear stress in plane C is the turbulent mixing layer generated downstream from the top of the cap. For $P = 20\%$, this turbulent mixing layer impacts the fine-sediment bed. It corresponds to the reattachment point located on the fine-sediment bed identified in the mean velocity fields. For larger protrusions, $P \geq 40\%$, the vertical turbulent mixing layer does not reach the fine-sediment bed anymore and impacts on the next spherical cap. The upper part of the mixing layer develops similarly for all the protrusion levels investigated, supporting the hypothesis that the form-induced sublayer is not strongly modified

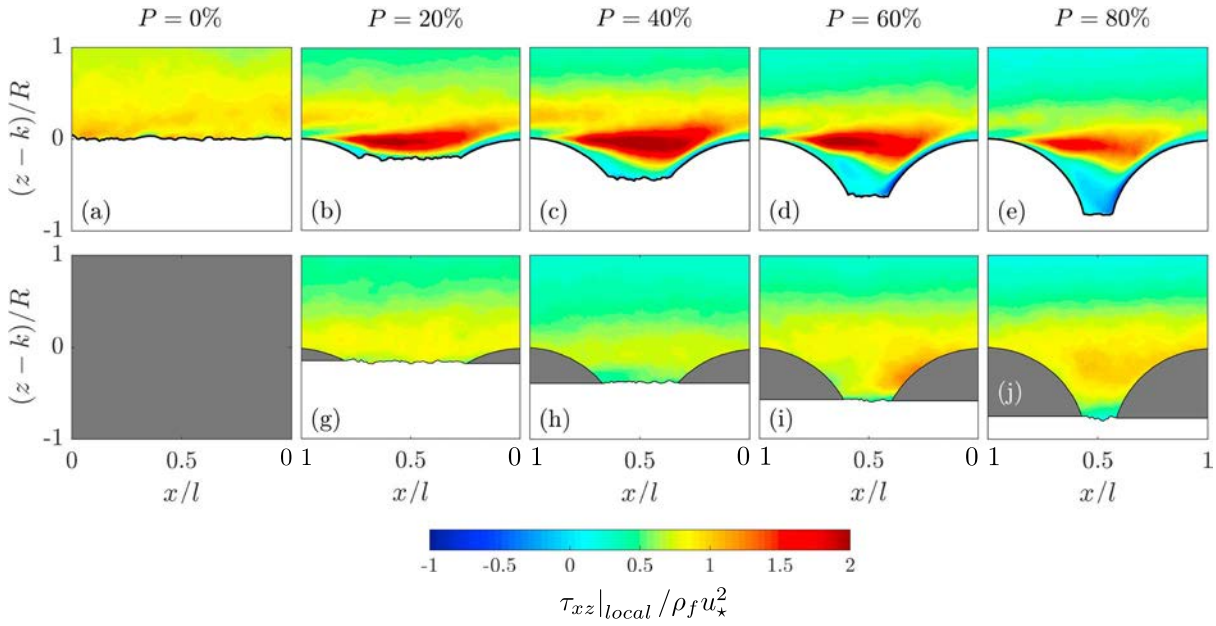

Figure 3. Dimensionless local shear stress $\tau_{xz}|_{\text{local}}/\rho_f u_\star^2$ for $Re_D = 27,700$ for the different protrusion levels. (a–e) Measurements in plane *C*. (g–j) Measurements in plane *A*. Gray areas are regions hidden from particle image velocimetry measurements.

with protrusion. However, the lower part of the mixing layer develops fully only for $P \geq 40\%$. For $P = 20\%$, the impact on the fine-sediment bed limits its growth. It can also be observed in Figure 3 that the magnitude of the normalized shear stress $\tau_{xz}|_{\text{local}}/\rho_f u_\star^2$ in the wake of the spherical caps decreases for $P > 40\%$. Yet it should be noted that this decrease of the normalized shear stress can be explained by a stronger increase of the friction velocity $\rho_f u_\star^2$ relative to a weaker increase of the shear stress $\tau_{xz}|_{\text{local}}$.

3.2. Double-Averaged Velocities and Spatially Averaged Turbulent Stresses

In the framework of the double-averaging methodology (e.g., Nikora et al., 2001), all time-averaged quantities $\bar{\psi}(x, y, z)$ are decomposed into a time-averaged and spatially averaged component $\langle\bar{\psi}\rangle$ and a dispersive component $\tilde{\psi}$, that is, $\bar{\psi} = \langle\bar{\psi}\rangle + \tilde{\psi}$, where the brackets $\langle.\rangle$ denote spatial averaging in the horizontal direction and the $\tilde{}$ denotes spacial fluctuation. Here the spatial averaging is performed over an elementary periodic pattern (see Figure 1a) since the roughness elements' distribution is periodic. In particular, the double-averaged quantities are estimated by averaging at a given level z the measurements in planes *A* and *C* between two caps' crests when caps are present or by averaging along the longitudinal direction in plane *C* for the no-protrusion case.

The resulting vertical profiles of the double-averaged longitudinal velocity $\langle\bar{u}\rangle$ are plotted in Figures 4a–4e for the five different protrusion levels and the three different Reynolds numbers. Above the caps ($z > k$), the longitudinal double-averaged velocity is well described by the logarithmic law:

$$\langle\bar{u}\rangle = \frac{u_\star}{\kappa} \ln\left(\frac{z-d}{k_s}\right) + B_r, \tag{4}$$

where $u_\star$ is the friction velocity at $z = k$ (discussed in section 3.3), d is the displacement height, k_s is the equivalent-sand-roughness scale, $\kappa = 0.41$ is the Von Kármán constant, and $B_r = 8.48$ for fully rough flows. The value of B_r was established by Nikuradse (1933) in order to obtain the correlation $k_s = d_{50}$ with natural sediment beds. The presence of a low velocity flow in the interfacial sublayer (below $z < k$) is obvious in the vertical profiles plotted in Figures 4a–4e. An inflection point can be identified for $P \geq 40\%$ near $z = k$, where the slope of the profiles reaches a local maximum. As for poorly sorted natural beds, the velocity profile deviates from the logarithmic form below the crests (Lamb et al., 2017; Wiberg & Smith, 1991). Wiberg and Smith (1991) conclude that the logarithmic profile starts somewhere between $z = d_{50}$ and d_{84} when the full size distribution of the bed is considered (i.e., both the fine and coarse sizes).

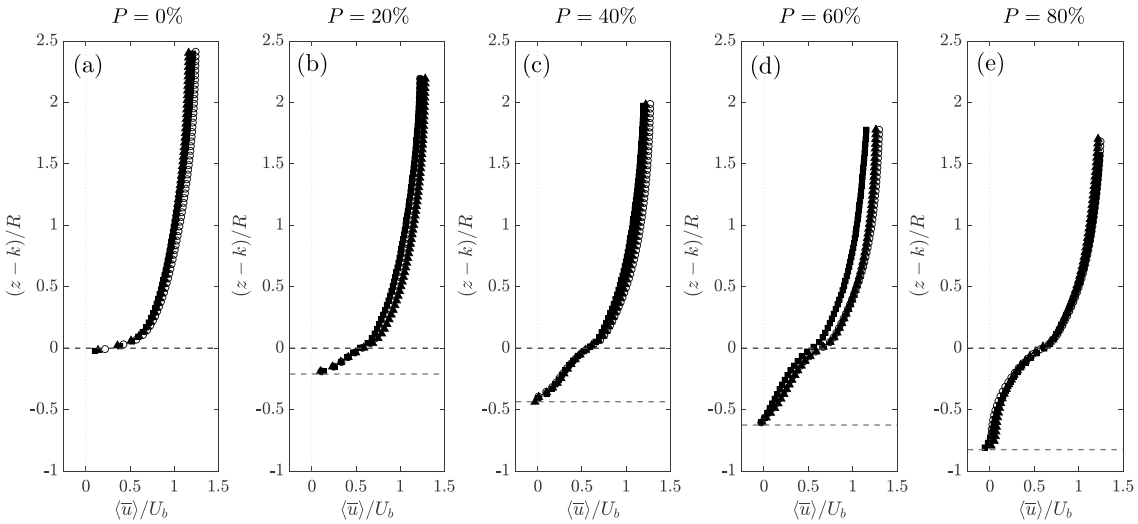

Figure 4. Vertical profiles of double-averaged longitudinal velocity $\langle\bar{u}\rangle$ for $Re_D = 27,700$ (black square), $Re_D = 18,600$ (empty circles) and $Re_D = 13,300$ (black triangle) and for (a) $P = 0\%$, (b) $P = 20\%$, (c) $P = 40\%$, (d) $P = 60\%$, and (e) $P = 80\%$. The horizontal dashed lines show the height of the spherical caps and the mean altitude of the glued fine sediment.

In the double-averaged longitudinal momentum equation, the total shear stress $\tau_{xz}(z)$ includes the dispersive (or form-induced) stress $-\rho_f\langle\tilde{u}\tilde{w}\rangle$. Thus, in the double-averaged framework, $\tau_{xz}(z)$ is given by

$$\tau_{xz}(z) = -\rho_f\langle\overline{u'w'}\rangle - \rho_f\langle\tilde{u}\tilde{w}\rangle + \mu\frac{\partial\langle\bar{u}\rangle}{\partial z}, \tag{5}$$

that is, the sum of the spatially averaged Reynolds shear stress, the dispersive shear stress, and the double-averaged viscous shear stress. More detail on the estimation of the dispersive stress is given in Florens et al. (2013) and Rouzes et al. (2018).

The vertical profiles of the total shear stress τ_{xz} for $Re_D = 27,700$ are plotted in Figures 5a–5e for the five different protrusion levels, respectively. For $P = 0\%$ (Figure 5a), the profile is linear as expected for a gravity-driven two-dimensional boundary layer. Also, for $P = 0\%$, τ_{xz} approaches 0 at $z/D = 0.4$, indicating

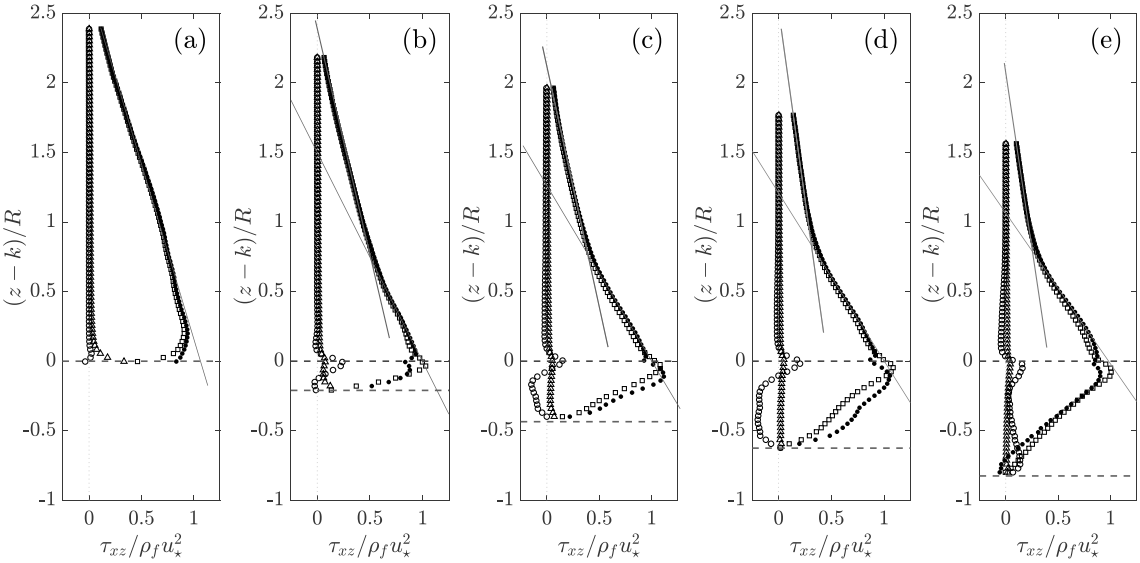

Figure 5. Vertical profiles of total shear stress $\tau_{xz}(z)$ (•), Reynolds shear stress $-\rho_f\langle\overline{u'w'}\rangle$ (□), viscous shear stress $\mu\langle\partial\bar{u}/\partial z\rangle$ (△), and dispersive shear stress $-\rho_f\langle\tilde{u}\tilde{w}\rangle$ (∘), for $Re_D = 27,700$ and (a) $P = 0\%$, (b) $P = 20\%$, (c) $P = 40\%$, (d) $P = 60\%$, and (e) $P = 80\%$. Linear fits of the lower and upper parts of the total shear stress, used to determine the height of the internal boundary layer, are plotted as gray straight lines. The horizontal dashed lines show the altitude of the spherical cap and the mean altitude of the glued fine sediment.

Table 2
Boundary Layer Parameters for All Regimes

Experiment	$P(\%)$	$\ell_z(m)$	δ_{IBL}/ℓ_z	$\delta_{\text{extrap}}/\ell_z$	d/ℓ_z	k_s/ℓ_z	h_{RS}/ℓ_z	z_m/ℓ_z	z_M/ℓ_z	z_m^ϵ/ℓ_z	z_M^ϵ/ℓ_z	$(\delta_{10\%}+d)/\ell_z$
P0Q14	0	0.0022	25.1	25.1	−0.24	1.14	0.50	1.11	2.07	0.67	3.38	6.2
P20Q14	20	0.0040	4.5	8.8	0.30	1.44	2.08	1.60	1.84	1.36	2.36	2.0
P40Q14	40	0.0080	2.8	4.2	0.64	1.02	2.75	1.36	1.46	1.22	1.75	1.6
P60Q14	60	0.0120	2.4	3.2	0.71	0.87	1.33	1.20	1.28	1.12	1.43	1.4
P80Q14	80	0.0160	1.9	2.4	0.74	0.86	1.69	1.12	1.17	1.08	1.28	1.4
P0Q9	0	0.0022	19.9	19.9	−0.05	1.30	0.64	3.25	3.60	2.56	4.65	6.9
P20Q9	20	0.0040	4.5	7.5	0.36	1.27	2.43	1.67	2.01	1.43	2.49	1.9
P40Q9	40	0.0080	2.8	3.9	0.65	1.06	2.38	1.39	1.53	1.22	1.82	1.7
P60Q9	60	0.0120	2.4	2.9	0.71	0.73	1.33	1.21	1.31	1.15	1.45	1.5
P80Q9	80	0.0160	1.9	2.3	0.78	0.74	1.63	1.15	1.22	1.10	1.33	1.4
P0Q7	0	0.0022	21.8	21.8	0.04	0.83	0.55	3.51	4.04	2.47	5.87	5.5
P20Q7	20	0.0040	4.5	7.2	0.38	1.27	3.75	1.72	1.96	1.43	2.58	2.1
P40Q7	40	0.0080	2.9	3.8	0.67	1.03	3.00	1.47	1.59	1.28	1.93	1.7
P60Q7	60	0.0120	2.3	2.8	0.74	0.56	1.42	1.23	1.32	1.15	1.47	1.4
P80Q7	80	0.0160	1.9	2.3	0.77	0.71	1.25	1.17	1.23	1.11	1.33	1.4

Note. ℓ_z is the vertical lengthscale of the rough bed, defined as equal to d_{50} for the no-protrusion case ($P = 0\%$) and equal to k, the protruded height, for all other protrusion levels ($P > 0\%$). The fitted logarithmic parameters are d, k_s as well as the lower and upper bounds z_m and z_M obtained by minimizing the slope error with initially five points, following the approach of Rouzes et al. (2018). z_m^ϵ and z_m^ϵ are the lower and upper bounds of the logarithmic law using a spatial convergence error estimate $\epsilon_{\langle\bar{u}\rangle}$ with 95% confidence. h_{RS} is the roughness sublayer height computed from the spatial standard deviation of the mean and turbulence statistics as in Florens et al. (2013) and Rouzes et al. (2018).

the top of boundary layer, which implies that the boundary layer developing on the fine sediment is not fully developed.

When the spherical caps protrude (Figures 5b–5e), the total shear stress profiles $\tau_{xz}(z)$ break into two linear slopes, the lower ones with a higher slope than the upper ones. In all cases, $\tau_{xz}(z)$ reaches a maximum value near the top of the spherical caps. The lower portions of the profiles with the stronger slopes reveal the development of a new boundary layer generated by the caps growing inside the upstream boundary layer generated by the fine-sediment bed. For $z < k$ below the caps' top, $\tau_{xz}(z)$ decreases, gradually reduced by the form and viscous drag induced by the caps and in accordance with the form and viscous drag terms in the double-averaged momentum equations inside the interfacial sublayer (e.g., Pokrajac et al., 2006).

The heights of the boundary layers developing on the patches were quantitatively determined using two approaches. The first height, noted δ_{extrap}, was obtained by extrapolating a linear fit of the lower portion of $\tau_{xz}(z)$ up to $\tau_{xz} = 0$. The second, noted δ_{IBL}, was defined by the level of the change of slope of $\tau_{xz}(z)$ and was obtained by the intersection of the linear fits of the lower and upper portions of $\tau_{xz}(z)$. In Figures 5b–5e, these linear fits have also been plotted.

The resulting boundary layer heights are given in Table 2, normalized by the height k of the spherical caps for $P > 0\%$ or by the small grain median diameter d_{50} for the no-protrusion case $P = 0\%$. For completeness, the prediction for the equilibrium layer thickness proposed by Cheng and Castro (2002) who studied the development of an internal boundary layer in an atmospheric-type boundary layer was also computed, noted $\delta_{10\%}$ (using equation $P10$ on Figure 10 of Cheng & Castro, 2002) by adding the displacement height d before normalizing with k, d being the altitude of the origin of the logarithmic section of the double-averaged longitudinal velocity. As seen in Table 2, $\delta_{10\%}$ gives the shortest estimations of the internal boundary layer height, followed by δ_{IBL} and δ_{extrap}. The heights will be discussed in section 3.4.

3.3. Logarithmic Law and Roughness Sublayer

The friction velocity $u_\star$ scaling the turbulence above the interfacial sublayer ($z > k$) is determined by extrapolating the total shear-stress profile to the top of the spherical caps ($z = k$) (Pokrajac et al., 2006; Rouzes et al., 2018). The roughness height k_s and the displacement height d are then determined by fitting a logarithmic law on the vertical profiles of the double-averaged longitudinal velocity of Figure 4, considering only the

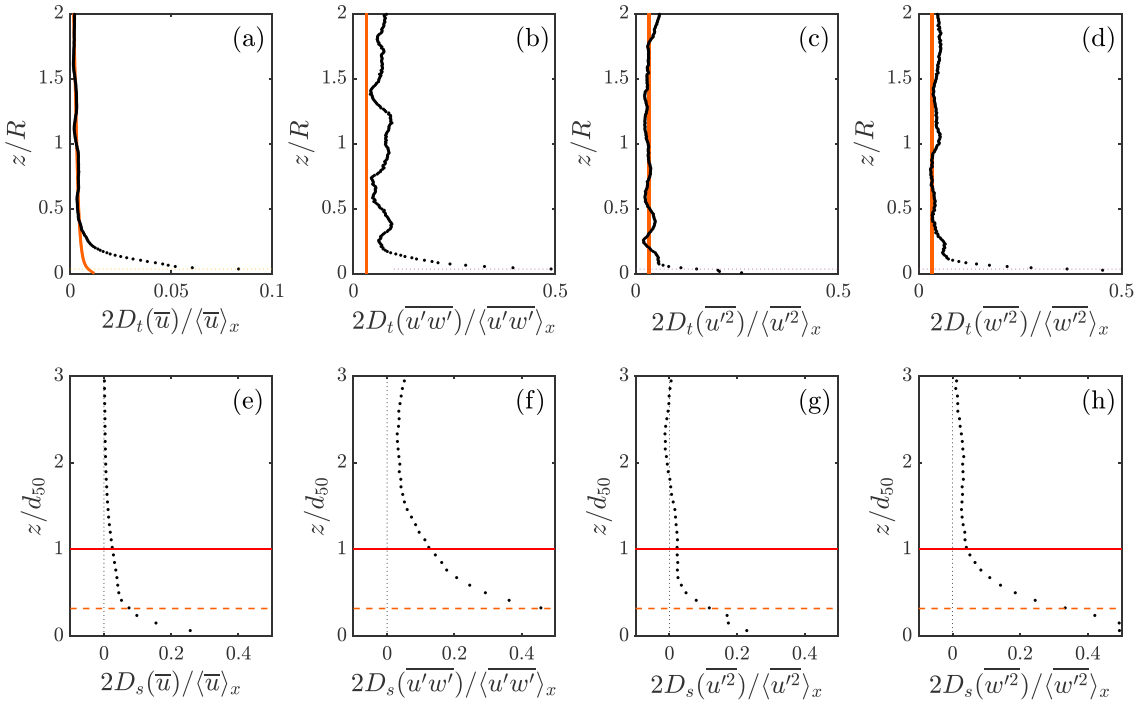

Figure 6. (a–d) Total spatial dispersion $2D_t$ (black dots) and time convergence error $\epsilon_{\bar{\psi}}$ (orange line), estimated here with a 95% confidence interval, for the protrusion level $P = 0\%$. The dotted horizontal lines show the altitude of the highest grain's top. (e–h) Spatial dispersion $2D_s$ for the protrusion level $P = 0\%$. The red line represents $z = d_{50}$, the altitude above the fine sediment chosen in the present study to estimate the bed flow conditions (see text). The dashed horizontal line shows the altitude of the highest grain's top.

region above the spherical caps ($z > k$) and following the constant κ method of Rouzes et al. (2018) with $\kappa = 0.41$. The values of the log law parameters $u_\star$, d, and k_s for the investigated regimes are given in Table 2, along with the lower and upper limits of the logarithmic law fit as defined and discussed in Rouzes et al. (2018).

The roughness sublayer for a turbulent flow over a rough bed is defined as the layer where the roughness elements induce mean-flow spatial heterogeneities. Following Florens et al. (2013) and Rouzes et al. (2018), the top of the roughness sublayer, noted h_{RS}, is defined as the height where the nondimensional spatial standard-deviation $2D_s(\bar{\psi}(z))/\langle\bar{\psi}(z)\rangle$ is equal to 5%. In order to remove the contribution of the time convergence error, Florens et al. (2013) showed that a good estimate of the spatial dispersion of a time-averaged quantity is given by

$$2D_s(\bar{\psi}(z)) = 2D_t(\bar{\psi}(z)) - \epsilon_{\bar{\psi}}, \tag{6}$$

where $D_t(\bar{\psi}(z)) = \sqrt{\langle\bar{\psi}^2(z)\rangle}$ is the total spatial dispersion based on the double-average decomposition, and $\epsilon_{\bar{\psi}}$ is the time convergence error of the turbulent quantities due to the finite number of independent samples used in the time averaging. The time convergence errors are estimated using the confidence intervals of the mean and variance of the velocity signals and the estimated number of independent samples. In the present study, h_{RS} is determined by the spatial standard deviation of the longitudinal mean velocity component, $2D_s(\bar{u}(z))/\langle\bar{\psi}(z)\rangle$. The normalized values for the different protrusion levels are given in Table 2.

The roughness sublayer for the no-protrusion case $P = 0\%$ deserves closer attention. The reason is that for the flows with emerging caps, two roughness sublayers coexist: one at the caps' scale and the other at the fine-sediment grain scale. In the next subsection, the spatial variations of the mean flow and turbulence quantities inside the cap's roughness sublayer will be investigated and must be distinguished from the spatial variations due to the fine grain roughness sublayer. Therefore, for $P = 0\%$, the total spatial dispersions $2D_t$ and the time convergence errors $\epsilon_{\bar{\psi}}$ are presented in Figures 6a–6d, for the relevant quantities, that is, the longitudinal velocity $\bar{u}$, the Reynolds shear stress $-\overline{u'w'}$, and the streamwise and vertical normal stresses $\overline{u'^2}$ and $\overline{w'^2}$. As in Florens et al. (2013), the total spatial dispersion $2D_t$ tends toward the time convergence error $\epsilon_{\bar{\psi}}$ at some level above the bed. The effective spatial dispersion $2D_s$ plotted in Figures 6e–6h shows that

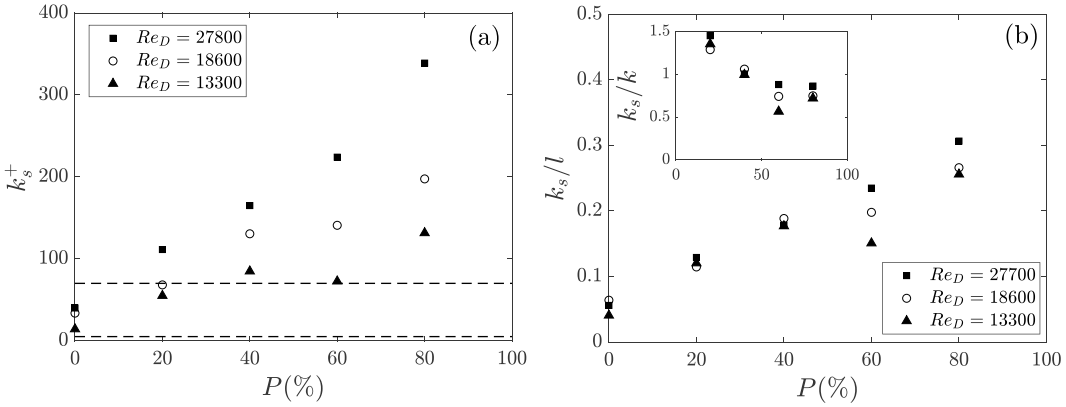

Figure 7. (a) k_s^+ of the patch plotted against the protrusion P. Dashed lines delimit the hydraulically smooth, transitional and rough bed. (b) Equivalent sand roughness k_s normalized by the distance between hemispheres plotted against the protrusion P. The inset shows the evolution of k_s normalized by the height of the spherical caps k.

$2D_s$, unlike $2D_t$, tends toward 0 at some level above the bed, in agreement with the concept of a roughness sublayer.

For the fine-sediment bed, the top of the roughness sublayer h_{RS} based upon the dispersion of the longitudinal mean velocity is roughly equal to $d_{50}/2$ (see Table 2). However, as seen in Figures 6e–6h, dispersion remains higher for other quantities, in particular for $-\overline{u'w'}$ (Figure 6f). By choosing a reference altitude at $z = d_{50}$ (red line in Figures 6e–6h), the spatial dispersion $2D_s$ at that level is below 5% for $\bar{u}$, $\overline{u'^2}$, and $\overline{w'^2}$, and below 10% for $-\overline{u'w'}$. Therefore, an altitude of $z = d_{50}$ above the fine-sediment bed appears to be a good compromise between the requirements of being out of the fine-sediment bed roughness sublayer and still remaining close enough to the fine-sediment bed to quantify the local forcing on the fine grains. This altitude will be used to calculate the flow quantities near the bed in the presence of protrusions.

3.4. Effect of Patch Protrusion on the Vertical Structure of the Turbulent Boundary Layer

In Table 2, it can be seen that the relative submergence of the roughness elements $\delta_{\text{extrap}}/l_z$ of the developing boundary layer over the glued sediment bed for the no-protrusion case $P = 0\%$ is very high with $\delta_{\text{extrap}}/l_z = \delta_{\text{extrap}}/d_{50}$ in the range $[19.9, 25.1]$ for the three Reynolds numbers investigated. As the caps protrude above the fine-sediment bed, the submergence of the caps relative to the cap-generated internal boundary layer decreases and drops to values as low as 1.9 for $P = 80\%$ using δ_{IBL} as the boundary layer thickness. For a similar array of cubes with roughly the same frontal density, Rouzes et al. (2018) showed that the logarithmic law is still found for relative submergence ratios down to 1.5, the mimimum ratio investigated, and that it extends deep into the roughness sublayer. Here logarithmic laws are also found, including for the lowest submergence, and located very close to the cap's top while penetrating the roughness sublayer (see Table 2). Moreover, for low submergence flows with $P \geq 40\%$, the top of the logarithmic law is in very good accordance with the thickness of the equilibrium layer predicted by Cheng and Castro (2002) and slightly smaller for the more submerged flow at $P = 20\%$.

The evolution of $k_s^+ = k_s u_\star/\nu$ with P is plotted in Figure 7a. $k_s^+ = k_s u_\star/\nu$ compares the equivalent-sand-roughness scale to the thickness of the viscous sublayer of the equivalent hydraulically smooth flow. For $P = 0\%$ and the three Reynolds numbers investigated, $5 < k_s^+ < 70$, showing that the bed is in the transitionally rough regime for the no-protrusion case. For $P = 20\%$, the bed becomes fully rough (i.e., $k_s^+ > 70$) for $Re_D = 27,700$ but stays in the transitional regime for smaller Reynolds numbers. For greater protrusion levels of the patch, the bed becomes fully rough for all the Reynolds numbers investigated.

The evolution of k_s/l with P is plotted in Figure 7b, where l is the distance between the hemisphere. For fully rough turbulent boundary layers, k_s is expected to be independent of the Reynolds number if the flow topology inside the roughness sublayer also remains the same. This is verified for $P = 20\%$ and $P = 40\%$ but not for $P = 60\%$ and $P = 80\%$. In Rouzes et al. (2018), a dependence of k_s with the relative submergence D/k is observed, but all estimations of the relative submergence in Table 2 (i.e., δ_{IBL}/k and δ_{extrap}/k) are almost Reynolds-number independent for a fixed value of P and cannot be responsible for the different values of k_s. Only a slight change of the flow topology in the roughness sublayer could explain this

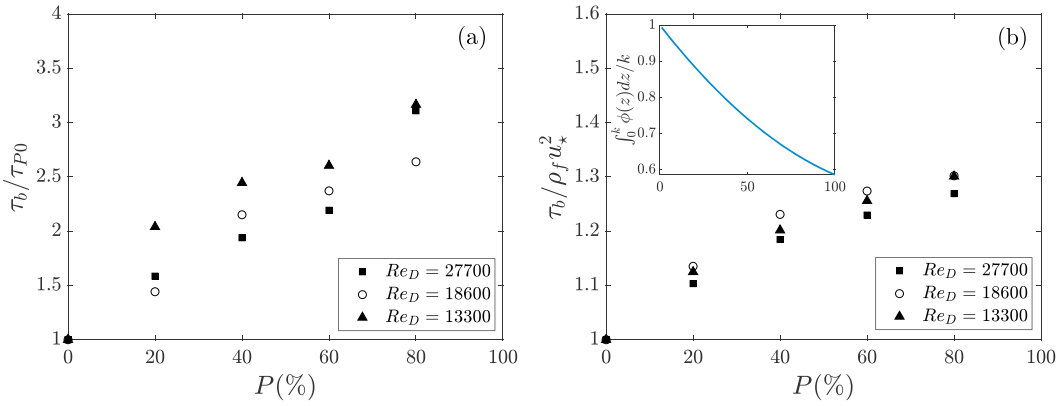

Figure 8. (a) Evolution of the ratio τ_b/τ_{P0} with the protrusion P. (b) Evolution of the ratio $\tau_b/\rho_f u_\star^2$ with the protrusion P. The inset shows the evolution of the integrated porosity $\int_0^k \phi(z)\mathrm{d}z/k$ with the protrusion P.

Reynolds number dependence. The flows around rounded objects like the present spherical caps are more subject to such dependence than roughness elements with sharp edges like cubes. However, the Reynolds number dependence does not mask the very clear trend in Figure 7b, where k_s/l increases linearly with the protrusion P.

As discussed in Rouzes et al. (2018), one of the difficulties with low relative-submergence flows over rough beds is that the friction velocity used to fit the logarithmic law, estimated at the top of the spherical caps, is different from the one yielding the bed shear stress τ_b which measures the total flow resistance in vertically integrated models. This bed shear stress associated with the total resistance of the bed (i.e., both the spherical caps and the fine-sediment bed) is given by (Pokrajac et al., 2006)

$$\tau_b = \rho_f u_\star^2 \left(1 + \left(\frac{\int_0^k \phi(z)\mathrm{d}z}{k}\right)\frac{k}{\delta_{\text{extrap}}}\right), \tag{7}$$

where $\phi(z)$ is the porosity of the bed, equal to 1 above the interfacial sublayer, and lower than 1 inside the interfacial sublayer. Profiles of $\phi(z)$ required to calculate τ_b depend of the protrusion P. At each level z, the intersection of the horizontal plane with a protruding hemisphere is considered. The surface of the intersected hemisphere is calculated analytically and substracted from the periodic pattern area l^2, yielding the fluid surface area at altitude z. The porosity at altitude z is then obtained by dividing this surface area by l^2.

The evolution of τ_b/τ_{P0} with protrusion P, where τ_{P0} is a reference value of τ_b corresponding to $P = 0\%$, is plotted in Figure 8a, and the evolution of $\tau_b/\rho_f u_\star^2$ is plotted in Figure 8b. The integral term in front of k/δ_{extrap} in equation (7) has been plotted as a function of the protrusion in the inset of Figure 8b. It corresponds to the bed-averaged porosity, noted Φ, of the rough bottom. It decreases from unity for $P = 0\%$ to 0.59 for $P = 100\%$, which is slightly larger than the value for a compact bed of spheres in a square arrangement (0.48). As the protrusion of the hemispheres increases, the drag acting on the caps becomes more important than the resistance of the fine-sediment bed and it can be seen accordingly in Figure 8a that τ_b/τ_{P0} increases, up to a ratio of 3 for $P = 80\%$. The ratio $\tau_b/\rho_f u_\star^2$ in Figure 8b is also seen to increase with P, reaching 1.3 for $P = 80\%$, but this is only due to the increasing low relative-submergence flow conditions, with δ_{IBL}/k ratios as low as 1.9 for $P = 80\%$. As seen in equation (7), for increasingly submerged flows as $k/\delta_{\text{extrap}} \to 0$, $\tau_b/\rho_f u_\star^2$ approaches 1.

4. Near-Bed Hydrodynamics

4.1. Determining the Local Shear Stress on the Fine-Sediment Bed

In this section, the fine-sediment shear stress τ_s, defined as the local shear stress acting on the bed of fine grains, is determined and compared to the total shear stress τ_b calculated from (7). The sediment shear stress τ_s is measured at the top of the rou ghness sublayer of the fine sediment (Nikora et al., 2001), that is, at $z = d_{50}$ as discussed in section 3.3. Below this level, the fine sediment induces spatial inhomogeneity of the

time-averaged quantities at the fine-grain scale. The local shear stress τ_s acting on the fine-sediment bed is therefore estimated by

$$\tau_s \equiv \tau_{xz}\big|_{\text{local}}(z = d_{50}) = \mu \left.\frac{\partial \bar{u}}{\partial z}\right|_{z=d_{50}} - \rho_f \left.\left(\overline{u'w'}\right)\right|_{z=d_{50}}. \quad (8)$$

Since the local shear stress is estimated at the top of the fine sediment's roughness sublayer, the dispersive stress is negligible. It should also be noted that estimating τ_s at $z = d_{50}$ above the fine-sediment bed might lead to small discrepancies for low relative submergence situations of the grains since the stress is not extrapolated to the bottom of the grains. However, in the following, the local shear stress will be always compared to the value of the bed shear stress taken at $z = d_{50}$ without spherical caps, that is, to τ_{P0}, to reveal the effect of the presence of spherical caps.

4.2. Spatial Distribution of the Fine-Sediment Shear Stress

Longitudinal profiles of the fine-sediment shear stress τ_s normalized by the total shear stress without spherical caps τ_{P0} are plotted in Figures (9a, 9c, and 9e) for plane C and in Figures (9b, 9d, and 9f) for plane A for all protrusion levels P and Reynolds numbers. When $\tau_s/\tau_{P0} < 1$, the fine sediment is locally sheltered from strong shear stress due the presence of the spherical caps. On the contrary, when $\tau_s/\tau_{P0} > 1$, the fine-sediment bed is locally exposed to the enhanced shear stress generated by the presence of the caps.

In plane A (see Figures 9b, 9d, and 9f), the shear-stress distribution on the fine-sediment bed is relatively uniform along the streamwise direction and is enhanced ($\tau_s/\tau_{P0} > 1$) by the caps for all protrusions, with a maximal enhancement for $P = 60\%$ at which τ_s/τ_{P0} reaches 1.9 for $Re_D = 27,700$ and 1.5 for $Re_D = 13,300$. Similar enhanced shear stress has been observed between two side-by-side cylinders (Kim et al., 2014), in the leeside of a row of cylinders (Sutton & McKenna Neuman, 2008a) or in an array of cylinders (Sutton & McKenna Neuman, 2008b). Kim et al. (2014) show that when the distance between the two cylinders is smaller than 2.5 times the diameter of the cylinders, the two horseshoe vortices developing on each cylinder can interact and create strong shear stress between the roughness elements. For an array of cylinders, Sutton and McKenna Neuman (2008b) explain that this effect persists if more rows of cylinders are present and that the effect of compression and acceleration of the flow between the roughness elements is additive. Here in the interfacial sublayer, the same process occurs: Even if the double-averaged longitudinal velocity is reduced by the drag of protruding caps, this global reduction hides an increase of the mean longitudinal velocity in plane A (which becomes a preferential path for the flow), enhancing the fine-sediment shear stress.

In plane C (see Figures 9a, 9c, and 9e), strong variations of τ_s/τ_{P0} along the streamwise direction are observed for all protrusions, with zones of sheltering and zones of enhanced shear stress developing between the caps. The length of the protection zone is very small for $P = 20\%$ but increases with P and leads to fine sediment exposed to reduced shear stress along the entire bed in plane C for $P = 60\%$ and $P = 80\%$. Similar sheltering zones were observed in the lee of an isolated hemisphere by Dixen et al. (2013). For $P = 20\%$, a zone of strongly enhanced fine-sediment shear stress is observed midway along the distance between the spherical caps, with τ_s/τ_{P0} reaching a maximum value of about 3 for the three Reynolds numbers investigated here. This strong enhancement is clearly associated with the impact on the fine-sediment bed of the mixing layer generated at the top of the caps, as observed in Figure 3b and discussed in section 3.1. For $P = 40\%$, a short distance of slightly enhanced shear stress appears close to the right spherical cap for $Re_D = 27,700$ and $Re_D = 18,600$ (see Figures 9a and 9c). For $Re_D = 13,300$, this enhancement disappears, with a maximum value similar to that without caps (see Figure 9e). The evolution of the horizontal profiles of τ_s/τ_{P0} in plane C corresponds to the transition observed with P in Figures 2a–2e and 3a–3e, where the reattachment points of the recirculation cell (and thus the impact of the mixing layer) shift from being located on the fine-sediment bed between successive caps ($P = 20\%$) to the front side of the downstream cap ($P \geq 60\%$). The $P = 40\%$ protrusion is an intermediate flow regime between these two situations, with a mixing-layer growth that still allows some enhancement of the fine-sediment shear stress: the reattachment point is already on the front side of the downstream cap but close enough to the fine bed sediment. The sediment is thus still influenced by the occurence of the mixing layer.

4.3. Spatial Distribution of the Near-Bed Turbulence Intensity

Sumer et al. (2003) showed how adding external near-bed turbulence to a flow can enhance grain entrainment. A way to take into account the level of turbulence for fine-sediment transport is to define the sediment

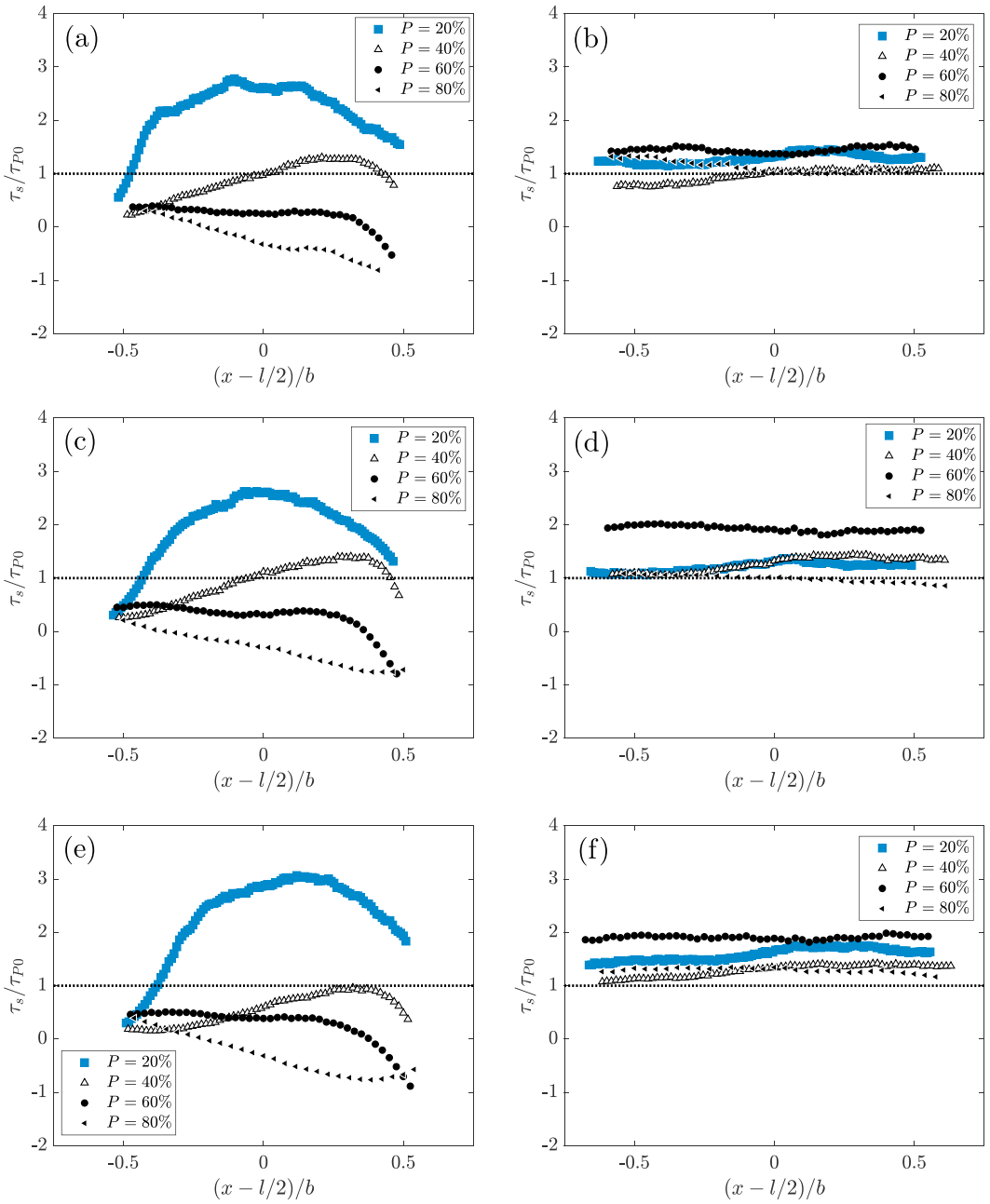

Figure 9. Horizontal profiles of fine-sediment shear stress τ_s between the spherical caps, normalized with the reference shear stress τ_{P0} (measured in the no-protrusion case $P = 0\%$) for all protrusion $P \geq 20\%$. $Re_D = 27,700$ in planes C (a) and A (b), $Re_D = 18,600$ in planes C (c) and A (d), and $Re_D = 13,300$ in planes C (e) and A (f). The longitudinal position is normalized by the spacing b at the base of protruding caps (Figure 1c).

shear stress directly via the turbulent kinetic energy near the fine-sediment bed TKE_s. With this approach, a new estimate for the fine-sediment shear stress, noted $\tau_{s,TKE}$ is given by

$$\tau_{s,TKE} = \rho_f C \quad TKE_s = \rho_f \frac{C}{2}\left(\overline{u'^2} + \overline{v'^2} + \overline{w'^2}\right), \tag{9}$$

where C is a constant. This constant is often chosen with a value equal to $C = 0.19$ (Nezu & Nakagawa, 1993; Soulsby, 1983) and corresponds to the amplitude of the exponential fits of the turbulent kinetic energy profiles in turbulent boundary layers when nondimensionalized by the friction velocity $u_\star$.

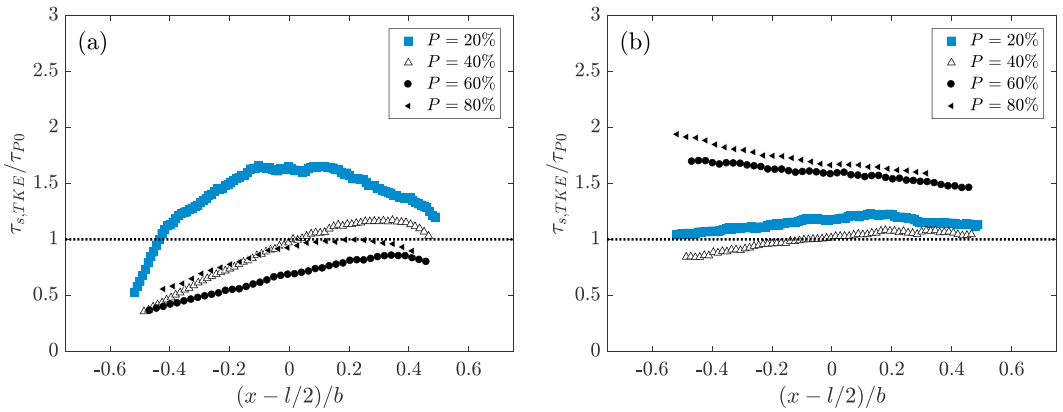

Figure 10. Horizontal profiles of fine-sediment shear stress $\tau_{s,TKE}$ estimated with the turbulent kinetic energy between the spherical caps and normalized with the reference shear stress τ_{P0} for all protrusion $P \geq 20\%$ for $Re_D = 27,700$ in (a) plane C and (b) plane A (Figure 1c).

Here the transverse velocity variance $\overline{v'^2}$ is not available, so that the turbulent kinetic energy is estimated following the suggestion of Nezu and Nakagawa (1993) with

$$TKE = \frac{1}{2}\frac{1}{0.72}\left(\overline{u'^2} + \overline{w'^2}\right). \tag{10}$$

It is then possible to determine the value of C from measurements without protrusion $P = 0\%$ at the level $z = d_{50}$ chosen to investigate the near-bed fine-sediment flow conditions. Thus, C with $TKE_s = \langle TKE \rangle (z = d_{50})$ evaluated for $P = 0\%$ is given by

$$C|_{PO} = \frac{\tau_{xz}(z = d_{50})}{\rho_f \langle TKE \rangle (z = d_{50})}. \tag{11}$$

For the three different Reynolds numbers investigated, $Re_D = \{13,300, 18,600, 27,700\}$, the values of $C|_{PO}$ are found to be 0.24, 0.25, and 0.26, respectively. Therefore, to estimate $\tau_{s,TKE}$ for $P \geq 20\%$ in equation (9), $C = 0.25$ was chosen for all P, with TKE_s evaluated at $z = d_{50}$.

Horizontal profiles of the fine-sediment shear stress $\tau_{s,TKE}$ calculated with the near-bed turbulent kinetic energy are plotted in Figures 10a and 10b for planes C and A, respectively, and normalized by τ_{PO}. The shape of these profiles for $P = 20\%$ and $P = 40\%$ are very similar to the shape of the profiles of τ_s/τ_{PO} in the corresponding Figures 9a and 9b. This indicates that for these flow regimes, both estimators reflect that the mixing layer impacts the fine-sediment bed ($P = 20\%$) or the next cap's toe (for $P = 40\%$), enhancing the near-bed fine-sediment shear stress in comparison with the no-protrusion case.

For $P \geq 60\%$, the two estimators give different yet complementary information in plane C. In Figure 9a, the fine-sediment shear stress τ_s/τ_{P0} is low and becomes highly negative near the toe of the downstream cap, in accordance with the downward motion of the recirculation there, suggesting a sheltering effect, since grains will tend to move upstream in such a flow. In Figure 10a, the fine-sediment shear stess $\tau_{s,TKE}/\tau_{PO}$ remains high for $P = 60\%$, with levels just below that of the no-protrusion case $P = 0\%$. This indicates that for $P \geq 60\%$, the instantaneous velocity fluctuations are still high enough in the wake of the caps to trigger grain motion, but since τ_s is then negative, this motion would then transport the grain upstream, toward more sheltered regions closer to the cap's lee face.

4.4. Double-Averaged and Maximum Near-Bed Fine-Sediment Shear Stress

Raupach et al. (1993) present a model for partitioning the bed shear stress τ_b between immobile roughness elements and the surrounding erodible bed. Their approach examines both the spatial average and the local maximum of the shear stress on the fine-sediment bed relative to the total shear stress (their equations (11) and (15), respectively). The method requires determining drag coefficients for the fine sediment C_S and the large roughness elements C_R. For $P = 0\%$, C_S can be calculated from

$$\tau_b(P = 0) = \rho_f C_S U_b^2, \tag{12}$$

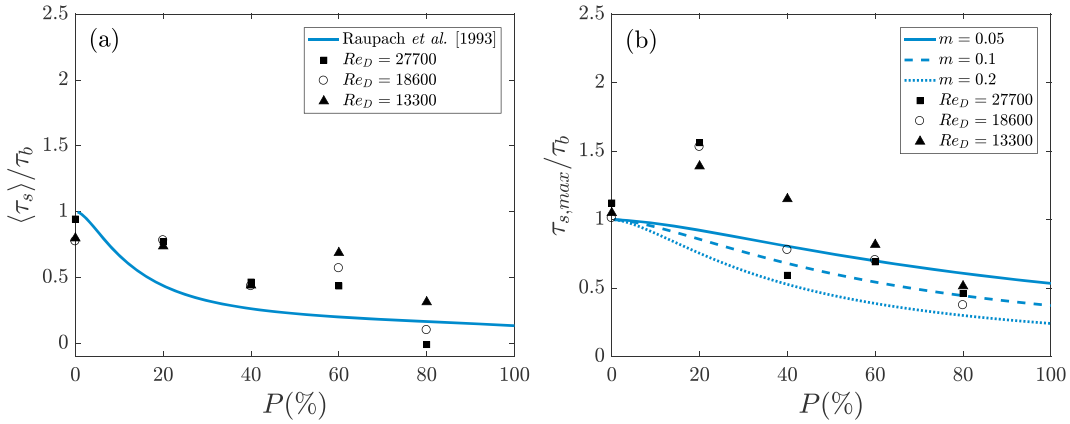

Figure 11. (a) Variation of the double-averaged value of the shear stress over the fine-sediment bed at $z = d_{50}$, normalized by the total bed shear stress. The blue line corresponds to the prediction based upon equation (11) of Raupach et al. (1993) for the shear stress averaged only on the fine-sediment surface (noted τ_s' in Raupach et al., 1993). (b) Variation of the maximum value of the shear stress over the fine-sediment bed at $z = d_{50}$, normalized by the total bed shear stress. The blue line corresponds to the computation of equation (15) of Raupach et al. (1993), with $C_R = 0.3$ and $m = 0.05, 0.1$ and 0.2.

which yields an average C_S value of 0.0050 ± 0.0007 for the three Reynolds numbers examined in our experiments. Values of C_R for the drag force on an isolated spherical cap could not be inferred from our measurements. Instead, $C_R = 0.3$ for full hemispheres was used as suggested by Raupach et al. (1993) and it was assumed that the drag coefficient is not dependent on the protrusion level of the spherical caps.

Two comparisons with the predictive model of Raupach et al. (1993) are possible here: the variation of the double-averaged shear stress acting on the finer sediment, $\langle \tau_s \rangle$, and the variation of the local maximum value of the shear stress acting on the finer sediment, $\tau_{s,\max}$. Figure 11a shows the evolution of the ratio $\langle \tau_s \rangle / \tau_b$ as a function of P. As the spherical caps protrude through the finer sediment, it appears that the part of the total bed shear stress effectively acting on the finer sediment decreases, with the shear stress on the fine-sediment bed being less than 30% of the total shear stress at $P = 80\%$ for all Reynolds numbers. This behavior is in good agreement with the predictive model of Raupach et al. (1993), both quantitatively and qualitatively. It should be noted though that the value of $\langle \tau_s \rangle$ measured here is only an approximate estimate of the double-averaged total shear stress near the finer sediment since the near bed flow in plane C is partially hidden by the spherical caps.

Figure 11b shows the evolution of $\tau_{s,\max}$ with P, normalized by the total bed shear stress τ_b. For $P = 0\%$, the experimental values of $\tau_{s,\max}/\tau_b$ are not strictly equal to unity. This is due to the time convergence error of the velocity measurements. Even at $z = d_{50}$, above the top of the fine sediment's roughness sublayer, there is still some spatial inhomogeneity in the streamwise direction, as seen in Figure 3a, scaling mainly with the time convergence error of $\epsilon_{-\overline{u'w'}}$ plotted in Figure 6b. For $P = 20\%$ though, $\tau_{s,\max}/\tau_b$ increases beyond 1, confirming the enhancement of the near-bed fine-sediment shear stress when the caps begin to protrude. It also shows that, locally, the fine-sediment shear stress can be far larger than the bed shear stress τ_b (which is spatially averaged horizontally). For $P > 20\%$, $\tau_{s,\max}/\tau_b$ decreases below unity. This trend is in accordance with the sheltering effect observed for high protrusions.

Raupach et al. (1993) introduced a parameter m in their model in order to take into account the spatial variability of the fine-sediment bed shear stress within the roughness sublayer of the coarser grains. m is used to infer $\tau_{s,\max}$ from $\langle \tau_s \rangle$. Predictions of the evolution of $\tau_{s,\max}$ with P, computed with the model of Raupach et al. (1993) using a constant value of C_R equal to 0.3 and three different values of the parameter m to predict $\tau_{s,\max}$ are shown in Figure 11b. Raupach et al.'s (1993) model with $m = 0.1$ can be seen to give the best agreement with the measurements, in particular for $P \geq 40\%$. However, the initial jump of $\tau_{s,\max}/\tau_b$ at $P = 20\%$ with shear stress ratios close to 1.5 is not predicted by any of the three values of m, nor by any other m values. Consequently, Raupach et al.'s (1993) model is not able to predict the intial increase of $\tau_{s,\max}/\tau_b$ that is observed in our experiments.

5. Discussion

Nickling and McKenna Neuman (1995) observed that when the roughness elements start to protrude above the fine-sediment bed, the grain entrainment first increases and then decreases when the roughness elements protrude more. Grams and Wilcock (2007) similarly observed that the entrainment rate of fine sediment was increased for protrusion levels of hemispheres in the range $0 < P(\%) < 50$. The results presented here quantify the two processes responsible for these observations. As the protrusion starts, both the near-bed fine-sediment shear stress τ_s and the near-bed turbulence intensity increase, associated with enhancement from strong sweep events (see Appendix A), explaining the increase of the entrainment rate for the available fine grains as observed in the above studies. This increase is so large (a jump of $\tau_{s,\max}/\tau_b$ toward values close to 1.5 and $\tau_{s,\max}/\tau_{P0}$ as large as 2.5 for $P = 20\%$ in Figure 9a) that it may not be compensated by the decrease of the fine-sediment bed area (fine-sediment availability) as the protrusion increases. Therefore, the total entrainment rate of fine sediment initially increases, as observed by Nickling and McKenna Neuman (1995) and Grams and Wilcock (2007). Then, as P increases further, the turbulence (Figure 10) and sweep events (Appendix A) generated by the spherical caps do not reach the fine-sediment bed. Combined with the decrease of the fine-sediment bed area, the drop of both the near-bed fine-sediment shear stress τ_s and the near-bed turbulence intensity below levels found before protrusion leads to a decrease of the entrainment rate of fine sediment as observed by Yager et al. (2007) and Grams and Wilcock (2007). In the present experiments with a square arrangement of closely spaced hemispheres, this protection of the fine-sediment bed in the lee of the hemispheres is reached for $P \geq 60\%$. This evolution of near-bed hydrodynamics with protrusion is in excellent accordance with the higher entrainment rate observed by Grams and Wilcock (2007) in the range $0 < P(\%) < 50$.

With a similar experimental setup, Papanicolaou et al. (2001) studied how varying the planar density of grains with a constant protrusion (fully protruded spherical elements) influences the time-averaged and instantaneous flow structure (using quadrant analysis as in Appendix A). In particular, the authors show that for a low density of coarse grains, quadrants 1 and 3 (Q_1 and Q_3) appear to dominate the flow, as a sign of energy being extracted from the turbulence to the mean flow. This is exactly what we measure here for the $P = 20\%$ case (see Appendix A). However, Papanicolaou et al. (2001) do not investigate the turbulent flow below the top of the coarse grains. The authors therefore cannot conclude on the penetration of the Q_1 and Q_3 events toward the finer sediment bed. Here the measurements show how this penetration disappears for large values of P (Figures A1 and A4).

Studies of fine-sediment transport over a layer of immobile coarse aggregates have generally made use of staggered configurations of hemispheres (Grams & Wilcock, 2007; Nickling & McKenna Neuman, 1995; Yager et al., 2007). Here a square configuration was chosen to enable PIV measurements within the interfacial sublayer. This choice leads to the presence of preferential alleys for the flow (plane A), where the enhancement and sheltering effects discussed above are not observed. Indeed, in these alleys, for all protrusions up to $P = 80\%$, the transport properties of the local flow conditions are enhanced by comparison with the no-protrusion flow. In staggered configurations, these alleys exist for low protrusions but disappear for high protrusions, raising the issue of whether our experiments apply to such configurations. For a square configuration, the separation in the transverse direction y between two aligned caps' crests, noted l', is the same as in the x direction, namely $l' = l$. Below the crests, the separation, noted b', depends on the protrusion according to $b' = l - 2R\sqrt{P(2-P)}$ so that the relative frontal area of the preferential alleys is $b'/l' = 1-2(R/l)\sqrt{P(2-P)}$. For a staggered configuration, l' is a bit lower than l, given by $l' = \sqrt{3}/2l$. Therefore, the relative frontal area of the preferential alleys is $b'/l' = 1 - 2(R/l)(4/\sqrt{3})\sqrt{P(2-P)}$. For $P = 20\%$ and $P = 40\%$, b'/l' is equal to 0.46 and 0.29, respectively, for the square configuration, and to 0.38 and 0.18, respectively, for the staggered configuration. For these low protrusions which correspond to the enhanced transport flow regimes, the preferential alleys are present in both configurations and occupy roughly the same area fraction. Thus, the present results and conclusions for $P = 20\%$ and 40% are likely to hold for both configurations. For $P = 60\%$, b'/l' is equal to 0.19 and 0.06 for the square and staggered configurations, respectively. For such levels of protrusion, the sheltering effect is effective in plane C along the caps' crests, and high values of the fine-sediment shear stress are found only in the preferential alleys (plane A). However, in a staggered configuration, such preferential alleys disappear as protrusion increases, with only a very small contribution to the flow rate remaining. Therefore, the results and conclusions for plane C are likely to hold even more strongly for a staggered configuration.

In experiments at constant discharge and constant water depth with a fine-sediment bed covering nonerodable hemispheres, one can expect, based on the present results, that when the hemispheres begin to protrude, the transport rate of the fine sediment initially increases then declines until a final protrusion level is reached for which the transport rate effectively stops. This final protrusion level depends on the initial transport rate but cannot be lower than the critical protrusion discussed in this paper, found to be about 40%, since for P less than about 40%, the transport rate is enhanced in comparison with the initial condition. Moreover, for $P > 40\%$, both the local bed shear stress τ_s and the turbulence stress near the fine-sediment bed $\tau_{s,TKE}$ decrease relatively quickly. The final protrusion level is then expected to be in the range [40%,60%] in experiments for which the flow conditions are initially just above the threshold for fine-sediment bed erosion. This explains why protrusions of around 50% are often observed in the literature (at least in experiments without bedforms, as pointed out by Grams & Wilcock, 2007).

6. Conclusion

This experimental study examined how the gradual protrusion of a patch of hemispheres from a fixed fine-sediment bed modifies the local hydrodynamics over the fine-sediment bed and, consequently, the ability of the flow to increase or decrease the fine-sediment motion.

As the protrusion starts (the first level examined is $P = 20\%$), the emerging hemispherical caps generate a vertical mixing layer which impacts the downstream fine-sediment bed. This impact locally increases both the near-bed fine-sediment shear stress τ_s and the near-bed turbulence intensity. For $P = 20\%$, the enhancement causes τ_s to be locally greater than both the spatially averaged bed shear stress $\langle \tau_s \rangle$ and the total bed shear stress τ_b, where the latter represents the hydraulic resistance of the flume bed, including the hemispherical caps and the fine sediment. A quadrant analysis (Appendix A) further reveals that this local enhancement consists of strong sweep events which are produced by the vertical mixing layer near the emergent crests of the caps. As the hemispheres' protrusion increases, the hydraulic roughness k_s also increases, approximately proportional to k, the cap's height. This increase of the hydraulic roughness of the bottom of the flume leads to a global increase of the friction and, therefore, of all relevant turbulence quantities (intensity and Reynolds shear stress), for a flow generated at constant depth D and discharge Q. For low protrusion, the two processes increase the ability of the flow to transport fine sediment.

The enhancement of the transport properties of the flow in the lee of the emerging caps only ceases when the turbulence and sweep events generated by the caps no longer reach the fine-sediment bed. In the present experiments with a square arrangement of closely spaced hemispheres, this protection of the fine-sediment bed in the lee of the hemispheres is reached for $P \geq 60\%$. For these high levels of protrusion, the fine-sediment shear stress drops below the zero-protrusion level, and the turbulence near the fine-sediment bed is essentially void of the sweep events generated near the caps' top and which are mostly responsible for grain movement. In experiments for which the flow conditions are initially just above the threshold for fine-sediment bed erosion, it is then not surprising that the final protrusion heights observed are never in the range $60\% \leq P \leq 100\%$.

Although the classical drag partition model of Raupach et al. (1993) is not able to reproduce the initial increase of the shear stress acting on the fine sediment for low values of P nor the transition to sheltering conditions for $P > 40\%$, it can still predict reasonably well the evolution of the maximum fine-sediment shear stress for $P \geq 60\%$ (with fitted parameters). This prediction of the evolution of the sediment shear stress and of the associated transport rate for $P \geq 60\%$ can then be used to estimate the protrusion height at which the fine-sediment shear stress becomes weaker than the critical shear stress as P increases from 60% to 100% (i.e., the point at which sheltering halts fine-sediment transport). This approach could be applied to experiments for which the flow conditions are initially very far above the threshold for fine-sediment bed erosion. For such flow conditions, the protection effect by the protruding hemispheres in the range $40\% \leq P < 60\%$ is not sufficient to stop sediment transport, and protrusion levels above $P \geq 60\%$ are necessary, in a range where the classical drag partition model of Raupach et al. (1993) is valid. New models need to be developed though to predict the fine-sediment shear stress distribution for the intermediate protrusions $0 < P < 50\%$.

Finally, it is noted that Trevisson (2016) observed that the erosion process of fine sediment around hemispheres exhibits two successive stages. In the first stage, erosion occurs at a fast rate, as explained above, then appears to stop at a protrusion level around 50%. However, in the second stage, erosion continues, but at a very low rate. In this stage, individual fine-sediment grains are put in motion only sporadically by

the near-bed turbulence and eventually find a way to move in the downstream direction along corridors between the large immobile grains. This second stage can be explained by the ability of turbulent structures in the interfacial sublayer flow to trigger grain motion even if the fine-sediment bed shear stress is below the classical threshold value (known only for simple boundary layer flows above uniform sediment beds). This mode of transport deserves further investigation but requires flow descriptions that focus not only on mean quantities but that also consider the instantaneous flow via quadrant or coherent structure analyses.

Appendix A: Quadrant Analysis

In order to quantify the nature of the events underlying the turbulent stresses and which affect the fine-sediment entrainment, a quadrant analysis was performed.

A.1. Joint Probability Distribution Functions for the Velocity

In order to classify the instantaneous events reaching the fine-sediment bed, a quadrant analysis was performed in a bed-parallel line at $z = d_{50}$ above the fine sediment. The joint probability density functions (JPDFs) of the fluctuating velocities (u', w') in plane C are shown in Figures A1a–A1e for the different protrusions P at $Re_D = 27,700$. For $P = 0\%$ (Figure A1a), the JPDF shows a strong presence of ejections (Q_2) with $u' < 0$ and $w' > 0$ and sweeps (Q_4) with $u' > 0$ and $w' < 0$ (Nolan et al., 2010). This reflects the presence of bursts classically observed above a rough bed (Sechet & le Guennec, 1999) with sweep events (Q4) found to be mainly responsible for fine-sediment transport (Nelson et al., 1995). Once the spherical caps appear, the shape of the JPDF is modified: For $P = 20\%$, the ellipse's angle increases, implying that the probability of Q_4 sweep events with higher negative vertical fluctuating velocities increases. If the fine sediments were set into motion, it is reasonable to assume that the fine-sediment rate would increase relative to the $P = 0\%$ case. The increased angle is in accordance with the observed increase of the maximum fine-sediment shear stress for $P = 20\%$, that is, a local increase of $-\overline{u'w'}$. For $P = 40\%$, the probability of having strong sweep events near the bed decreases and the ratio between the two joint PDF ellipse axes approaches unity, revealing that strong instantaneous events barely reach the fine-sediment bed anymore. Finally, at $P = 60\%$, the

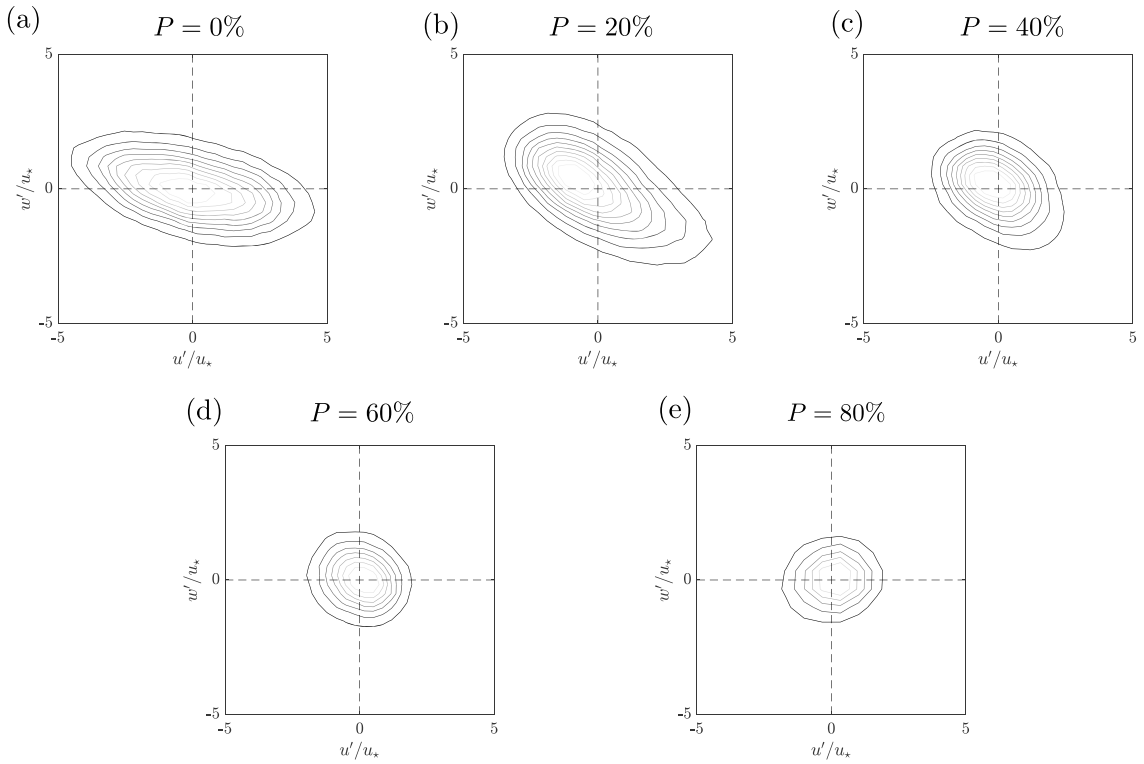

Figure A1. Joint probability density functions of the fluctuating velocities in a horizontal line at $z = d_{50}$ above the fine-sediment bed in plane C and $Re_D = 27,700$: (a) $P = 0\%$, (b) $P = 20\%$, (c) $P = 40\%$, (d) $P = 60\%$, and (e) $P = 80\%$.

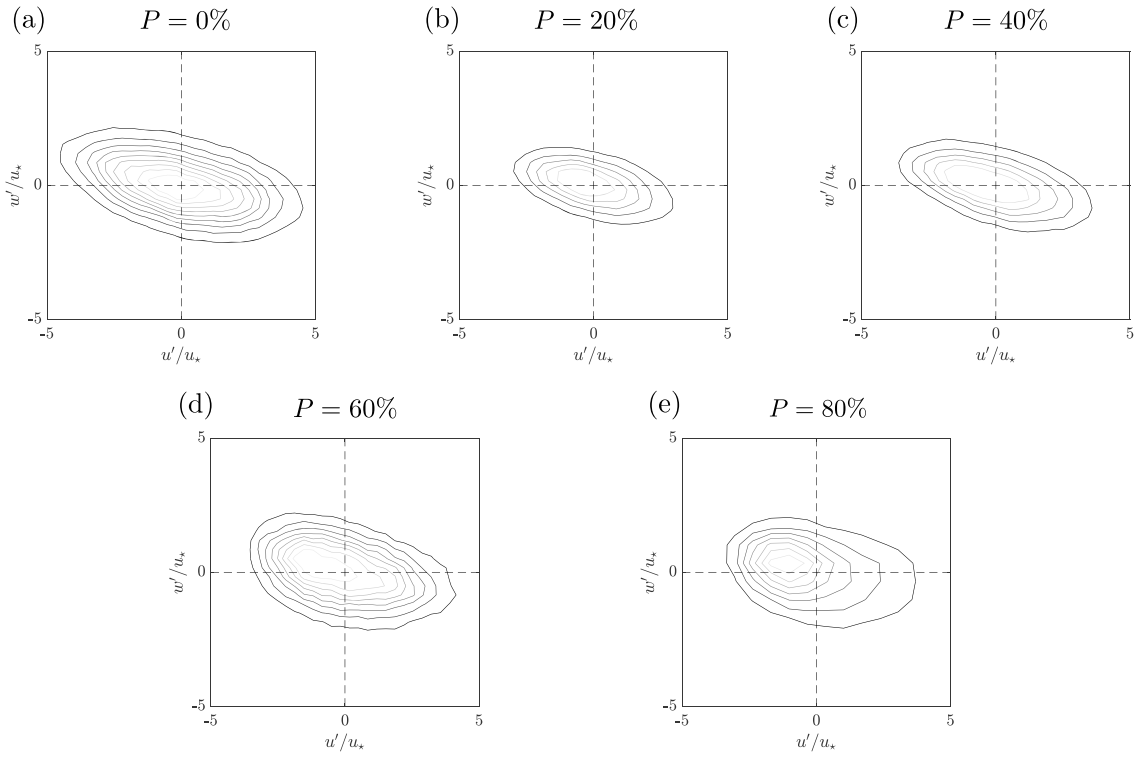

Figure A2. Joint probability density functions of the fluctuating velocities in a horizontal line at $z = d_{50}$ above the fine-sediment bed in plane A for $Re_D = 27,700$ and (a) $P = 0\%$, (b) $P = 20\%$, (c) $P = 40\%$, (d) $P = 60\%$, and (e) $P = 80\%$.

JPDF becomes essentially circular, that is, the turbulence becomes nearly isotropic with $-\overline{u'w'}$ approaching 0. Also, the fluctuating velocities decrease.

Figure A2 shows the JPDFs at $z = d_{50}$ in plane A. It can be seen that the sweep event generation is less modified by increasing P than in plane C. For all P, the JPDFs of the fluctuating velocities near the bed, although distorted, remain ellipsoidal with strong probabilities of ejections and sweeps.

A.2. Space-Averaged Residual Shear Stress

In order to understand which instantaneous events have the most influence on the near bed shear stress and how their contributions to the total bed shear stress vary with the protrusion of the spherical caps, the residual shear stress introduced by Raupach (1981) was computed. In particular, in each plane, a spatially averaged residual shear stress ΔS as a function of z was computed, defined by

$$\Delta S = \frac{|\langle \overline{u'w'}_2 \rangle_x| - |\langle \overline{u'w'}_4 \rangle_x|}{\langle \overline{u'w'} \rangle_x}, \tag{A1}$$

where $\overline{u'w'}_2$ and $\overline{u'w'}_4$ are the quadrant-selective time-averages of either Q_2 (ejections) or Q_4 (sweep) events, respectively.

Vertical profiles of the x-averaged residual shear stress in plane C are plotted in Figures A3a–A3e with black dotted lines for all P, respectively. For $P = 0\%$, it appears that near the fine-sediment bed, the sweeps and ejection events contribute approximately equally to the total Reynolds shear stress, in good agreement with Mignot et al. (2009) for gravel beds. Above the top of highest grain, the residual shear stress increases continuously from 0 (see Figure A3a), implying that ejection events contribution increases relatively to sweeps, that is, that Q_4 events become scarcer further up from the bed.

For $P \geq 20\%$ in plane C, the residual shear stress profiles are strongly modified. For all $P \geq 20\%$, it appears that ejection events contribute more than sweeps to the total Reynolds shear stress above the spherical caps ($z > k$) and that sweeps contribute more to the Reynolds stress beneath the spherical caps' top (the interfacial layer). This is in good agreement with the observation of Nezu and Sanjou (2008) in a vegetated canopy,

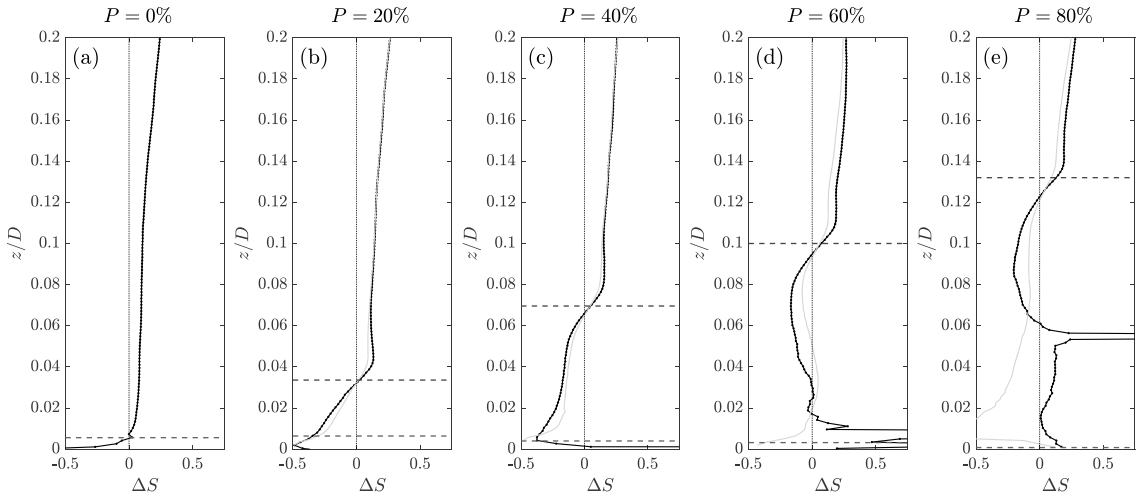

Figure A3. Residual shear stress between sweeps and ejections spatially averaged in the x direction in plane C (black dotted lines) and in plane A (gray lines) for $Re_D = 27,700$: (a) $P = 0\%$, (b) $P = 20\%$, (c) $P = 40\%$, (d) $P = 60\%$, and (e) $P = 80\%$. Dashed lines represent the top of the spherical caps and the top of the highest fine-sediment grain.

who show that at the inflection point of the double-averaged velocity profile, the shear instability generates ejection and sweeps events. These inflection points are easily seen to be located near the cap's top $z = k$ in Figure 4.

The main difference between the different protrusion levels investigated here is the nature of events that reach the fine-sediment bed, visible in the variation of the near-bed residual shear stress with P in Figures A3a–A3e. For $P = 20\%$, the residual shear stress decreases toward a values close to -0.5 near the fine-sediment bed, showing that the sweep events generated at the inflection point of the velocity profile still have a strong influence on the fine-sediment shear stress. For $P = 40\%$, the residual shear stress reaches an almost constant value of around -0.2 in the interfacial sublayer and is still as low as -0.4 near the fine-sediment bed. For $P \geq 60\%$ though, the strong sweep events generated around the inflection point near the cap's top do not reach the fine-sediment bed anymore, the decrease of the residual shear stress in the upper region of the interfacial sublayer being erased by a return to values close to 0 in the lower part, when approaching the fine-sediment bed. To conclude, the contribution of Q_4 sweep events near the bed increases for small protrusion and decreases for greater protrusion.

Vertical profiles of the x-averaged residual shear stress in plane A are also plotted in Figures A3a–A3e, in gray, for all P, respectively. In this plane, sweep events near the fine-sediment bed remain dominant (negative values of the residual shear stress) for all P. This is consistent with the persistence of the elliptical shape in the JPDFs of the velocity fluctuations near the bed.

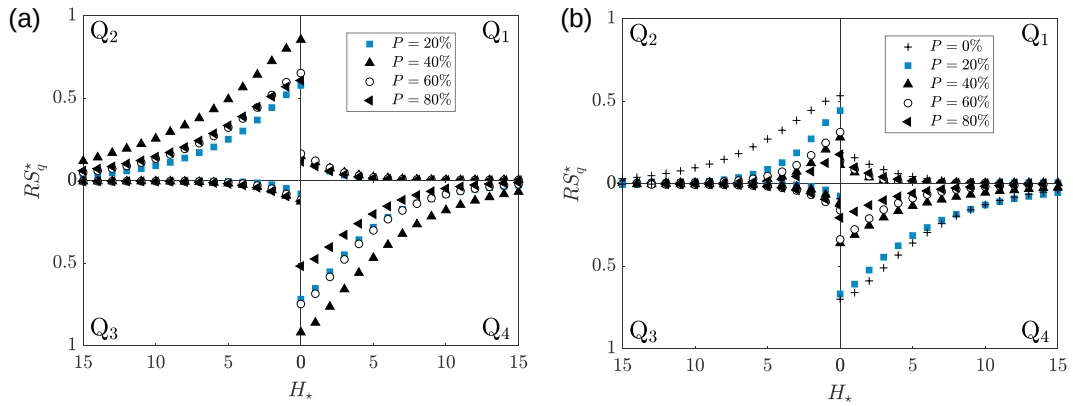

Figure A4. Contribution of each quadrant to the total Reynolds stress plotted as a function of the hole size for a hole based on a multiple $H_\star$ of the friction velocity for $Re_D = 27,700$: (a) at the spherical cap's top $z = k$ and (b) at $z = d_{50}$.

A.3. Threshold-Level Dependence of the Reynolds Stress

Extreme events are defined as instantaneous fluctuating velocities stronger than a multiple of the mean shear stress. These events, even if rare, are the ones that have the highest probability to set grains in motion. A quadrant hole analysis is therefore performed in order to investigate how extreme events reaching the fine-sediment bed are modified with the protrusion of the spherical caps. In the literature, the quadrant hole analysis is usually performed by defining a threshold as a multiple H of the Reynolds stress taken locally at the analysis position, or as a multiple H of the Reynolds stress averaged in space at the analysis height.

In the current study, the goal is to investigate how events generated near the top of the hemispheres penetrate and reach the fine-sediment bed. To this end, a threshold based on a multiple $H_\star$ of the friction velocity (defined at the top of the caps, and not at the analysis height as in the classical approach) is used. Following Mignot et al.'s (2009) notations, the contribution of one quadrant to the total Reynolds is then defined as

$$RS_q^\star(z, H_\star) = \frac{1}{N}\sum_{n=1}^{N}\gamma_\star(z,n)D_\star(\gamma_\star), \tag{A2}$$

where

$$\gamma_\star(z,n) = \frac{u'w'(z,n)}{u_\star^2}, \tag{A3}$$

$$D_\star(\gamma_\star) = \begin{cases} 1 \text{ for } |\gamma_\star| \geq H_\star \text{ and } \gamma_\star \text{ in the quadrant } q. \\ 0 \text{ otherwise} \end{cases} \tag{A4}$$

At $z = k$, the top of the caps, the use of the classical hole threshold H or the friction velocity hole threshold $H_\star$ used here yield almost similar results. At $z = d_{50}$ for the near-bed analysis, the use of the friction velocity hole threshold $H_\star$ allows one to determine more easily if the extreme events detected are those generated at $z = k$, by simply comparing the results at the two altitudes. The quantities above are then double-averaged using measurements in both planes A and C . It should be noted that the single-plane x average of Mignot et al. (2009) is equivalent to a double average since longitudinal variations are considered equivalent to lateral ones.

Figure A4a gives the evolution with P of the double-averaged Reynolds stress associated with each quadrant as a function of the hole size $H_\star$ at the spherical cap's top in plane C for $Re_D = 27,700$. For all P, it appears that quadrants Q_2 and Q_4 still contribute to the total Reynolds stress for $H_\star > 5$, while Q_1 and Q_3 do not contribute to the total Reynolds stress for $H_\star > 5$. This observation has been already made in the outer flow over a rough bed by Raupach (1981). It reflects the fact that extreme events generated at the roughness elements top are mainly sweeps and ejections.

For the same plane and Reynolds number, Figure A4b shows the evolution at $z = d_{50}$. For all P, it can be seen that for $H_\star > 5$, the quadrants Q_1 and Q_3 do not contribute anymore to the total Reynolds stress as for $z = k$. One can also observe that the presence of strong Q_4 events near the bed is heavily dependent on the protrusion level of the hemispheres. For $P \geq 40\%$, Q_4 approaches zero contribution to the total Reynolds stress for $H_\star \approx 10$, while for $P = 20\%$, Q_4 events are measured up to $H_\star = 15$.

For $P = 20\%$, the similarity of the Q_4 sweep events between Figures A4a and A4b, both qualitatively and quantitatively, indicates that essentially all sweep events generated near the cap's top are reaching the fine-sediment bed, resulting in an increased probability to set the fine-sediment grains into motion.

Acknowledgments

The authors thank S. Cazin, M. Marchal, and G. Freche for their valuable support and help with the experiments, and the AFB (French Agency for Biodiversity) who funded this work and the PhD of David Raus. We also thank the reviewers for their constructive remarks which helped to improve this paper. All experimental data used in this paper are part of a Zenodo open data file (https://doi.org/10.5281/zenodo.2575568).

References

Al-Awadhi, J. M., & Willetts, B. B. (1999). Sand transport and deposition within arrays of non-erodible cylindrical elements. *Earth Surface Processes and Landforms*, *24*(5), 423–435. https://doi.org/10.1002/(SICI)1096-9837(199905)24:5<423::AID-ESP998>3.0.CO;2-E

Chang, W. Y., Constantinescu, G., Tsai, W. F., & Lien, H. C. (2011). Coherent structure dynamics and sediment erosion mechanisms around an in-stream rectangular cylinder at low and moderate angles of attack. *Water Resources Research*, *47*, W12532. https://doi.org/10.1029/2011WR010586

Cheng, H., & Castro, I. P. (2002). Near-wall flow development after a step change in surface roughness. *Boundary-Layer Meteorology*, *105*(3), 411–432.

Dixen, M., Sumer, B. M., & Fredsøe, J. (2013). Numerical and experimental investigation of flow and scour around a half-buried sphere. *Coastal Engineering*, *73*, 84–105. https://doi.org/10.1016/j.coastaleng.2012.10.006

Einstein, H. A, & Banks, R. B. (1950). Fluid resistance of composite roughness. *AGU Transactions*, *31*, 603–610. https://doi.org/10.1029/TR031i004p00603

Ferguson, R. I. (2012). River channel slope, flow resistance, and gravel entrainment thresholds. *Water Resources Research*, *48*, W05517. https://doi.org/10.1029/2011WR010850

Florens, E., Eiff, O., & Moulin, F. (2013). Defining the roughness sublayer and its turbulence statistics. *Experiments in Fluids*, *54*(4), 1500.

Gillette, D. A., & Stockton, P. H. (1989). The effect of nonerodible particles on wind erosion of erodible surfaces. *Journal of Geophysical Research*, *94*(D10), 12,885–12,893. https://doi.org/10.1029/JD094iD10p12885

Gillies, J. A., Nickling, W. G., & King, J. (2006). Aeolian sediment transport through large patches of roughness in the atmospheric inertial sublayer. *Journal of Geophysical Research*, *111*, f02006. https://doi.org/10.1029/2005JF000434

Graba, M., Moulin, F. Y., Boulêtreau, S., Garabétian, F., Kettab, A., Eiff, O., et al. (2010). Effect of near-bed turbulence on chronic detachment of epilithic biofilm: Experimental and modeling approaches. *Water Resources Research*, *46*, W11531. https://doi.org/10.1029/2009WR008679

Grams, P., & Wilcock, P. (2007). Equilibrium entrainment of fine sediment over a coarse immobile bed. *Water Resources Research*, *43*, W10420. https://doi.org/10.1029/2006WR005129

Grams, P., & Wilcock, P. (2014). Transport of fine sediment over a coarse, immobile riverbed. *Journal of Geophysical Research: Earth Surface*, *119*, 188–211. https://doi.org/10.1002/2013JF002925

Grimmond, C. S. B., & Oke, T. R. (1999). Aerodynamic properties of urban areas derived from analysis of surface form. *Journal of Applied Meteorology*, *38*(9), 1262–1292. https://doi.org/10.1175/1520-0450(1999)038<1262:APOUAD>2.0.CO;2

Hardy, R., Best, J., Lane, S., & Carbonneau, P. (2010). Coherent flow structures in a depth-limited flow over a gravel surface: The influence of surface roughness. *Journal of Geophysical Research*, *115*, F03006. https://doi.org/10.1029/2009JF001416

Iversen, J. D., Wang, W. P., Rasmussen, K. R., Mikkelsen, H. E., & Leach, R. N. (1991). *Roughness element effect on local and universal saltation transport* (pp. 65–75). Vienna: Springer Vienna.

Kim, H. S., Nabi, M., Kimura, I., & Shimizu, Y. (2014). Numerical investigation of local scour at two adjacent cylinders. *Advances in Water Resources*, *70*, 131–147.

Lamb, M. P., Brun, F., & Fuller, B. M. (2017). Hydrodynamics of steep streams with planar coarse-grained beds: Turbulence, flow resistance, and implications for sediment transport. *Water Resources Research*, *53*, 2240–2263. https://doi.org/10.1002/2016WR019579

Marshall, J. (1971). Drag measurements in roughness arrays of varying density and distribution. *Agricultural Meteorology*, *8*, 269–292. https://doi.org/10.1016/0002-1571(71)90116-6

Mignot, E., Barthelemy, E. E., & Hurther, D. (2009). On the structure of shear stress and turbulent kinetic energy flux across the roughness layer of a gravel-bed channel flow. *Journal of Fluid Mechanics*, *638*, 423–452. https://doi.org/10.1017/S0022112009990772

Morris, H. M. (1955). Flow in rough conditions. *Transactions ASCE*, *120*, 373–398.

Nelson, J. M., Schmeeckle, M. W., & Shreve, R. L. (2001). Turbulence and particle entrainment. In M. P. Mosley (Ed.), *Gravel-bed rivers* (Vol. V, pp. 240–241). Wellington, New Zealand: New Zealand Hydrol. Soc.

Nelson, J. M., Shreve, R. L., McLean, S. R., & Drake, T. G. (1995). Role of near-bed turbulence structure in bed load transport and bed form mechanics. *Water Resources Research*, *31*(8), 2071–2086. https://doi.org/10.1029/95WR00976

Nezu, I., & Nakagawa, H. (1993). *Turbulence in open channel flows*: Taylor and Francis.

Nezu, I., & Sanjou, M. (2008). Turburence structure and coherent motion in vegetated canopy open-channel flows. *Journal of Hydro-environment Research*, *2*(2), 62–90. https://doi.org/10.1016/j.jher.2008.05.003

Nickling, W. G., & McKenna Neuman, C. (1995). Development of deflation lag surfaces. *Sedimentology*, *42*(3), 403–414. https://doi.org/10.1111/j.1365-3091.1995.tb00381.x

Nikora, V., Goring, D., McEwan, I., & Griffiths, G. (2001). Spatially averaged open-channel flow over rough bed. *Journal of Hydraulic Engineering*, *127*(2), 123–133. https://doi.org/10.1061/(ASCE)0733-9429(2001)127:2(123)

Nikuradse, J. (1933). Strömungsgesetze in rauhen Rohren, VDI-Forschungsheft 361, Beilage zu “Forschung auf dem Gebiete des Ingenieurwesens”, Ausgabe B Band 4, Juli/August1933.

Nolan, K. P., Walsh, E. J., & McEligot, D. M. (2010). Quadrant analysis of a transitional boundary layer subject to free-stream turbulence. *Journal of Fluid Mechanics*, *658*, 310–335. https://doi.org/10.1017/S0022112010001758

Papanicolaou, A. N., Diplas, P., Dancey, C. L., & Balakrishnan, M. (2001). Surface roughness effects in near-bed turbulence: Implications to sediment entrainment. *Journal of Engineering Mechanics*, *127*(3), 211–218. https://doi.org/10.1017/S0022112010001758

Pokrajac, D., Finnigan, J., Manes, C., McEwan, I., & Nikora, V. (2006). On the definition of the shear velocity in rough bed open channel flows. *Proceedings of the International Conference on Fluvial Hydraulics - River Flow, 2006*, 89–98.

Raupach, M. R. (1981). Conditional statistics of Reynolds stress in rough-wall and smooth-wall turbulent boundary layers. *Journal of Fluid Mechanics*, *108*, 363–382. https://doi.org/10.1017/S0022112081002164

Raupach, M. R. (1992). Drag and drag partition on rough surfaces. *Boundary-Layer Meteorology*, *60*(4), 375–395. https://doi.org/10.1007/BF00155203

Raupach, M. R., Gillette, D. A., & Leys, J. F. (1993). The effect of roughness elements on wind erosion threshold. *Journal of Geophysical Research*, *98*(D2), 3023–3029. https://doi.org/10.1029/92JD01922

Rouzes, M., Moulin, F. Y., Florens, E., & Eiff, O. (2018). Low relative-submergence effects in a rough-bed open-channel flow. *Journal of Hydraulic Research*, *57*, 1–28. https://doi.org/10.1080/00221686.2018.1478894

Schneider, J. M., Rickenmann, D., Turowski, J. M., & Kirchner, J. W. (2015). Applicability of bed load transport models for mixed size sediments in steep streams considering macroroughness. *Water Resources Research*, *51*, 5260–5283. https://doi.org/10.1002/2014WR016417

Sechet, P., & le Guennec, B. (1999). The role of near wall turbulent structures on sediment transport. *Water Research*, *33*(17), 3646–3656. https://doi.org/10.1016/S0043-1354(99)00072-X

Smith, J. D., & McLean, S. R. (1977). Spatially averaged flow over a wavy surface. *Journal of Geophysical Research*, *82*(12), 1735–1746. https://doi.org/10.1029/JC082i012p01735

Soulsby, R. (1983). Chapter 5 the bottom boundary layer of shelf seas. In B. Johns (Ed.), *Physical oceanography of coastal and shelf seas*, Elsevier Oceanography Series (Vol. 35, pp. 189–266). Elsevier. https://doi.org/10.1016/S0422-9894(08)70503-8

Sumer, B. M., Chua, L. H. C., Cheng, N.-S., & Fredsøe, J. (2003). Influence of turbulence on bed load sediment transport. *Journal of Hydraulic Engineering*, *129*(8), 585–596. https://doi.org/10.1061/(ASCE)0733-9429(2003)129:8(585)

Sutton, S. L. F., & McKenna Neuman, C. (2008a). Sediment entrainment to the lee of roughness elements: Effects of vortical structures. *Journal of Geophysical Research*, *113*, F02S09. https://doi.org/10.1029/2007JF000783

Sutton, S. L. F., & McKenna Neuman, C. (2008b). Variation in bed level shear stress on surfaces sheltered by nonerodible roughness elements. *Journal of Geophysical Research*, *113*, f03016. https://doi.org/10.1029/2007JF000967

Trevisson, M. (2016). Experimental study of erosion of particles in a rough bed (masters thesis), Karlsruhe Institut für Technologie.

Wiberg, P. L., & Smith, J. D. (1991). Velocity distribution and bed roughness in high-gradient streams. *Water Resources Research*, *27*, 825–838. https://doi.org/10.1029/90WR02770

Wren, D. G., Langendoen, E. J., & Kuhnle, R. A. (2011). Effects of sand addition on turbulent flow over an immobile gravel bed. *Journal of Geophysical Research*, *116*, f01018. https://doi.org/10.1029/2010JF001859

Yager, E. M., Kirchner, J. W., & Dietrich, W. E. (2007). Calculating bed load transport in steep boulder bed channels. *Water Resources Research*, *43*, W07418. https://doi.org/10.1029/2006WR005432